

Deciphering Lyman α blob 1 with deep MUSE observations[★]

Edmund Christian Herenz^{1,2}, Matthew Hayes², and Claudia Scarlata³

¹ European Southern Observatory, Av. Alonso de Córdova 3107, 763 0355 Vitacura, Santiago, Chile
e-mail: eherenz@eso.org

² Department of Astronomy, Stockholm University, AlbaNova University Centre, SE-106 91, Stockholm, Sweden

³ Minnesota Institute for Astrophysics, School of Physics and Astronomy, University of Minnesota, 316 Church Str. SE, Minneapolis, MN 55455, USA

November 28, 2021

ABSTRACT

Context. Lyman α blobs (LABs) are large-scale radio-quiet Lyman α ($\text{Ly}\alpha$) nebula at high- z that occur predominantly in overdense proto-cluster regions. Especially the prototypical SSA22a-LAB1 at $z = 3.1$ has become an observational reference for LABs across the electromagnetic spectrum.

Aims. We want to understand the powering mechanisms that drive the LAB to gain empirical insights into galaxy formation processes within a rare dense environment at high- z . Thus we need to infer the distribution, the dynamics, and the ionisation state of LAB 1's $\text{Ly}\alpha$ emitting gas.

Methods. LAB 1 was observed for 17.5 h with the VLT/MUSE integral-field spectrograph. We produced optimally extracted narrow band images in $\text{Ly}\alpha$ $\lambda 1216$, He II $\lambda 1640$, and we tried to detect C IV $\lambda 1549$ emission. By utilising a moment based analysis we mapped the kinematics and the line profile characteristics of the blob. We also linked the inferences from the line profile analysis to previous results from imaging polarimetry.

Results. We detect $\text{Ly}\alpha$ emission to surface-brightness limits of $10^{-19} \text{ erg s}^{-1} \text{ cm}^{-2} \text{ arcsec}^{-2}$. At this depth we reveal a bridge between LAB 1 and its northern neighbour LAB 8, as well as a shell-like filament towards the south of LAB 1. Complexity and morphology of the $\text{Ly}\alpha$ profile vary strongly throughout the blob. Despite the complexity, we find a coherent large scale east-west $\sim 1000 \text{ km s}^{-1}$ velocity gradient that is aligned perpendicular to the major axis of the blob. We detect He II emission in three distinct regions, but we can only provide upper limits for C IV .

Conclusions. Various gas excitation mechanisms are at play in LAB 1: Ionising radiation and feedback effects dominate near the embedded galaxies, while $\text{Ly}\alpha$ scattering is contributing at larger distances. The $\text{He II}/\text{Ly}\alpha$ ratios combined with the upper limits on $\text{C IV}/\text{Ly}\alpha$ ratios favour shock models over photo-ionisation. The alignment of the angular momentum vector parallel to the morphological principal axis appears odds with the predicted norm for high-mass halos, but likely reflects that LAB 1 resides at a node of multiple intersecting filaments of the cosmic web. LAB 1 can thus be thought of as a progenitor of present day massive elliptical within a galaxy cluster.

Key words. Cosmology: observations – Galaxies: high-redshift – Galaxies: haloes – Techniques: imaging spectroscopy

1. Introduction

Lyman α ($\text{Ly}\alpha$) blobs (LABs) are very luminous ($L_{\text{Ly}\alpha} \gtrsim 10^{43.5} \text{ erg s}^{-1}$) and very extended ($\gtrsim 10^2 \text{ kpc}$ in projection) $\text{Ly}\alpha$ emitting nebulae. They were unexpectedly revealed in narrow-band imaging campaigns targeting Lyman α emitting galaxies (LAEs) at $z \gtrsim 3$ (Steidel et al. 2000, see also Francis et al. 1996). LABs have now been found in numerous, sometimes LAB-dedicated, high- z galaxy surveys (e.g. Matsuda et al. 2004; Nilsson et al. 2006; Prescott et al. 2012, 2013). Their presence is confirmed from $z \sim 1$ (Barger et al. 2012) up to $z \sim 7$ (Ouchi et al. 2009; Sobral et al. 2015; Shibuya et al. 2018; Zhang et al. 2019). Moreover, a very rare class of extended $z \sim 0.3$ [O III] nebulae have been proposed to share similarities with high-redshift LABs (Schirmer et al. 2016).

The distinctive observational feature of LABs with respect to likewise extended and luminous high- z $\text{Ly}\alpha$ nebulae around radio-galaxies (e.g. Morais et al. 2017; Vernet et al. 2017;

Marques-Chaves et al. 2019), radio-loud quasars (e.g. Smith et al. 2009; Roche et al. 2014), or radio-quiet quasars (e.g. Husemann et al. 2018; Arrigoni Battaia et al. 2019; Drake et al. 2019) is that the primary powering source driving their $\text{Ly}\alpha$ emission is usually not detected or not obvious from the rest-frame UV and rest-frame optical discovery data (see also review by Cantalupo 2017, and references therein). However, the defining physical characteristic of LABs is their preferential occurrence within overdense high- z proto-cluster regions. In fact, already the first LABs were found in narrow-band searches targeting known or presumed high-density structures (Francis et al. 1996; Steidel et al. 2000). Following these initial discoveries, other narrow-band surveys targeting redshift overdensities were able to replicate the success in unveiling LABs (e.g. Palunas et al. 2004; Erb et al. 2011; Mawatari et al. 2012; Cai et al. 2017; Kikuta et al. 2019). Conversely, also LABs found in blind searches could be linked to over-densities (Prescott et al. 2008; Yang et al. 2009, 2010; Bădescu et al. 2017). Given that their preferred habitats are proto-cluster regions and their sizes are enormous it appears natural to suspect LABs as the progenitors of extremely massive, if not the most-massive galaxies in present day cluster environments (see also review by Overzier 2016).

[★] Based on observations made with ESO Telescopes at the La Silla Paranal Observatory under programme ID 094.A-0605, programme ID 095.A-0570, and programme ID 097.A-0831.

The required amount of hydrogen ionising photons to drive the observed Ly α output of the blobs via recombinations is $\dot{Q}(h\nu \geq 13.6\text{ eV}) \gtrsim 10^{55}\text{ s}^{-1}$ for a $L_{\text{Ly}\alpha} \gtrsim 10^{44}\text{ erg s}^{-1}$ LAB in a standard case-B recombination scenario. This \dot{Q} would correspond to star-formation rates $\gtrsim 100\text{ M}_{\odot}\text{ yr}^{-1}$ and absolute UV magnitudes $M_{\text{UV}} < -23$ using canonical conversion factors (e.g. Kennicutt 1998). The absence of such bright UV galaxies in the vicinity of the nebulae may indicate that the powering source(s) are heavily dust-obscured along the line of sight. Moreover, it might also hint at an additional source of Ly α photons in LABs, namely collisional excitations of neutral hydrogen by free electrons, a process which also cools the heated electron gas. As a coolant, Ly α is most effective for gas temperatures around 10^4 K . In the case of LABs potential heating sources could be star-burst driven superwinds from the heavily obscured central galaxies (e.g. Taniguchi & Shioya 2000; Mori et al. 2004) or the gravitational potential of the halo hosting the blob (“gravitational cooling”, e.g. Haiman et al. 2000; Rosdahl & Blaizot 2012).

The gravitational cooling mechanism was initially deemed the dominant powering source for driving Ly α emission from LABs (Haiman et al. 2000; Dijkstra & Loeb 2009). This idea is especially intriguing, as theoretical models predict that gas accretion onto galaxies forms dense cold flow filaments (e.g., Kereš et al. 2005; Dekel & Birnboim 2006; Brooks et al. 2009; Stewart et al. 2017). Despite its theoretical importance, empirical evidence for this processes in high- z galaxies remains circumstantial (e.g. Rauch et al. 2016). The filamentary Ly α morphology as well as the alignment of their major axes with the surrounding large scale structure are regarded as observational support for the gravitational cooling scenario.

The polarisation of the observed Ly α emission from the blob could potentially distinguish between the central engine hypothesis or the in-situ powering by gravitational cooling (Dijkstra & Loeb 2008; Eide et al. 2018). In the former case the polarisation fraction is expected to increase with distance from the embedded sources. And indeed, for Lyman α blob 1, the object examined in detail in this study, such a polarisation signature was detected (Hayes et al. 2011; Beck et al. 2016). While these observations were initially thought to be inconsistent with the in-situ production of Ly α photons by gravitational cooling, Trebitsch et al. (2016) showed that gravitational cooling may imprint a polarisation signature that is consistent with the observations (see also Sect. 2).

Nevertheless, follow-up campaigns with X-ray, sub-mm, IR, and radio-facilities revealed that a significant fraction of LABs harbour indeed highly obscured star-bursts with star-formation rates $\sim 10^2 - 10^3\text{ M}_{\odot}\text{ yr}^{-1}$ or AGNs (e.g. Yang et al. 2011; Ao et al. 2015, 2017). Thus, mechanical heating and/or ionising radiation from these buried systems are definitely contributing and possibly dominating the energy budget that powers Ly α in LABs. The filamentary morphology can in such a scenario still be reconciled with the cooling flow scenario, as those flows are expected to fuel star-formation and AGN activity in the first place. But rather than being lit-up in Ly α by gravitational cooling, these filamentary flows could simply be illuminated from the systems that they are feeding (Prescott et al. 2015b). However, according to Dijkstra & Loeb (2009), a potential counter-argument to this scenario is that the gas in the cold flows is self-shielded from ionising radiation given the expected typical densities ($n_{\text{H}} > 1\text{ cm}^{-3}$). Moreover, it appears counter-intuitive that the heavily obscured embedded sources have high escape fractions of ionising photons into large enough solid angles to power the blobs. As of yet, there is still no consensus on the importance of the possible Ly α powering mechanisms in LABs.

Disentangling the different Ly α powering mechanisms at work in LABs is warranted, as the relevant Ly α emission processes are linked to the physical processes that regulate the build-up of stellar mass and growth of super-massive black holes in the most-massive galaxies of the present day universe. Integral-field spectroscopic (IFS; Bacon & Monnet 2017) observations are an especially promising observational line of attack for such studies. The modern integral-field spectrographs on 10 m class telescopes, i.e. the “Keck Cosmic Web Imager” (Morrissey et al. 2018) at the Keck II telescope and the “Multi Unit Spectroscopic Explorer” (MUSE, Bacon et al. 2010, 2014) at ESO’s Very Large Telescope UT4, are ideally suited to cover the projected sizes of LABs. An analyses of combined spectral and spatial information from IFS can provide a detailed view of the Ly α morphokinematics. Especially, cold-mode accretion filaments are expected to leave imprints on the velocity fields compared to simple Keplerian motions (Arrigoni Battaia et al. 2018; Martin et al. 2019). Moreover, gas which is not affected by star-formation or AGN driven feedback is expected to be kinematically more quiescent than feedback heated gas. Thus these processes can potentially be distinguished by spatially mapping the observed Ly α line width.

A difficulty in interpreting line-of-sight velocities and line-widths from Ly α emission, is that resonant scattering diffuses the intrinsic Ly α radiation field in real and frequency-space (see review by Dijkstra 2019). The spatial diffusion can be envisioned as a projected smoothing processes (Bridge et al. 2018), that can enhance the apparent size of the Ly α blobs by reducing the steepness of their surface brightness profiles (Zheng et al. 2011; Gronke & Bird 2017). Moreover, it can also “wash-out” cold-accretion features of small angular size (Smith et al. 2019). The diffusion in frequency space, which is dependent on the kinematics and column densities of the scattering medium, can lead to significant modulations of the spectral profile (e.g., Laursen et al. 2009). Additionally, the transmission of the Ly α photons through the intergalactic medium will also modify the line profile (e.g., Laursen et al. 2011). However, the observed low-velocity shifts of rest-frame optical emission lines with respect to Ly α for some of the galaxies associated with the LABs are at odds with the expectations from Ly α radiative transfer theory (e.g. McLinden et al. 2013). This might indicate that Ly α scattering does not significantly modulate the observable velocity field of LABs. Thus it is possible to obtain a measure the angular momentum of the gas in the early formation stage of a massive haloe, which directly relates to the action of tidal torques from the surrounding large scale structure and the cosmic web (see e.g. Forero-Romero et al. 2014; Lee et al. 2018, and references therein).

Further insights into the thermodynamic properties of the emitting gas of $z \sim 3$ blobs can be gained from ground based IFS data due to the potential detectability of other rest-frame UV emission lines. Especially He II $\lambda 1640$ and C IV $\lambda 1550$ emission have been used as diagnostics for LABs (Prescott et al. 2009; Scarlata et al. 2009a; Arrigoni Battaia et al. 2015). Both lines act as gas-coolants, but for a higher temperature ($T \approx 10^5\text{ K}$) gas phase compared to Ly α which cools the 10^4 K phase (Yang et al. 2006). Heating sources driving this phase could be feedback effects from the embedded galaxies (Mori et al. 2004; Cabot et al. 2016) or the gravitational potential of the halo hosting the blob (Yang et al. 2006; Dijkstra & Loeb 2009). However, both lines can also be powered by photo-ionisation, but require the abundance of higher energy photons to produce the recombining species. Such hard ionising radiation is only expected in the vicinity of extremely low metallicity stellar populations (see, e.g. review by Schaerer 2013) or near an AGN (e.g. Humphrey et al.

2019). Analysing relative line strengths and comparing the spatial distribution of the He II and C IV emitting gas to the positions of potential ionising sources within blob may help to distinguish between photo-ionisation and cooling-radiation scenarios.

With the aim to decipher the physical processes at work in LABs we present here the so-far deepest obtained IFS observations of a giant $z \sim 3$ LAB. Our target is the prototypical giant Steidel et al. LAB – SSA-22a Lyman α blob 1 (LAB1). LAB 1 lives in one of the most overdense regions known at $z = 3.1$. This region, referred to as the SSA 22 proto-cluster, shows a significant density peak of Lyman break galaxies (Steidel et al. 1998, 2003; Saez et al. 2015), Lyman α emitting galaxies (LAEs, Hayashino et al. 2004; Yamada et al. 2012), sub-mm galaxies (Tamura et al. 2009), AGNs (Lehmer et al. 2009b; Alexander et al. 2016), and also LABs (Matsuda et al. 2004, 2011). Interestingly, with an estimated cluster mass of $2\text{--}4 \times 10^{14} M_{\odot}$, the SSA 22 proto-cluster may actually be an unique structure within the horizon (Kubo et al. 2015).

Since its discovery LAB 1 became the target of numerous follow up observations and is thus the most well studied LAB to-date. We will provide an overview of those results in the following Sect. 2 before describing our new 17.2 h MUSE observations of LAB 1 in Sect. 3. In Sect. 4 we detail how we reduced the MUSE data. We present our analysis and results in Sect. 5, and in Sect. 6 we discuss the interpretations of our findings. Lastly, we summarise and present our conclusions in Sect. 7.

Throughout the paper we assume a canonical 737-cosmology, i.e. $\Omega_{\Lambda} = 0.7$, $\Omega_M = 0.3$, and $H_0 = 70 \text{ km s}^{-1} \text{ Mpc}^{-1}$. Adopted reference line wavelengths stem from the atomic line list compiled by van Hoof (2018), all wavelengths $< 2000 \text{ \AA}$ refer to vacuum wavelengths, and for conversions between air- and vacuum wavelengths we follow the prescriptions adopted in the Vienna Atomic Line Database (Ryabchikova et al. 2015).

2. Summary of previous results on LAB 1

LAB 1 (RA: 22h17m26.0s, Dec: +00°12'36") was originally discovered in a narrow-band image by Steidel et al. (2000). These observations targeted Ly α emission of a previously identified redshift overdensity at $z = 3.1$ (Steidel et al. 1998) that was revealed as a peak in the redshift distribution of a spectroscopic follow-up campaign for Lyman break selected galaxies in the SSA-22 field (Steidel et al. 1998). With an isophotal area of 181 arcsec^2 (10523 kpc^2 in projection) and a total Ly α luminosity of $8.1 \times 10^{43} \text{ erg s}^{-1}$ LAB 1 still remains the largest and one of most luminous LABs known (Matsuda et al. 2011). Directly north of LAB 1, offset by $\approx 12''$ from its photometric centre, Matsuda et al. (2004) identified a companion blob: LAB 8 (RA: 22h17m26.1s, Dec: +00°12'55", $L_{\text{Ly}\alpha} = 1.5 \times 10^{43} \text{ erg s}^{-1}$, isophotal area 40 arcsec^2). However, as will be demonstrated in the present analysis (Sect. 5) this structure merges with LAB 1 at lower surface brightness limits.

Two of the Lyman break galaxies from Steidel et al. (1998) are within the combined LAB 1 / LAB 8 structure. Adopting the nomenclature of Steidel et al. (2003), these are SSA22a-C11 and SSA22a-C15. We list the coordinates of both galaxies in Table 1¹. SSA22a-C11 is located in the south-west of LAB 1,

¹ We note the coordinates for these Lyman break galaxies provided in Steidel et al. (2003) – RA=22h17m25.67s/Dec=+00°12'35.2" for SSA22a-C11, and RA=22h17m26.127s/Dec=+00°12'55.3" for SSA22a-C15 – appear to be offset by $\sim 1''$ to the north-west with respect to where these galaxies are located in our data. As described in Sect. 4.2, we aligned our data with the 2MASS reference frame, while

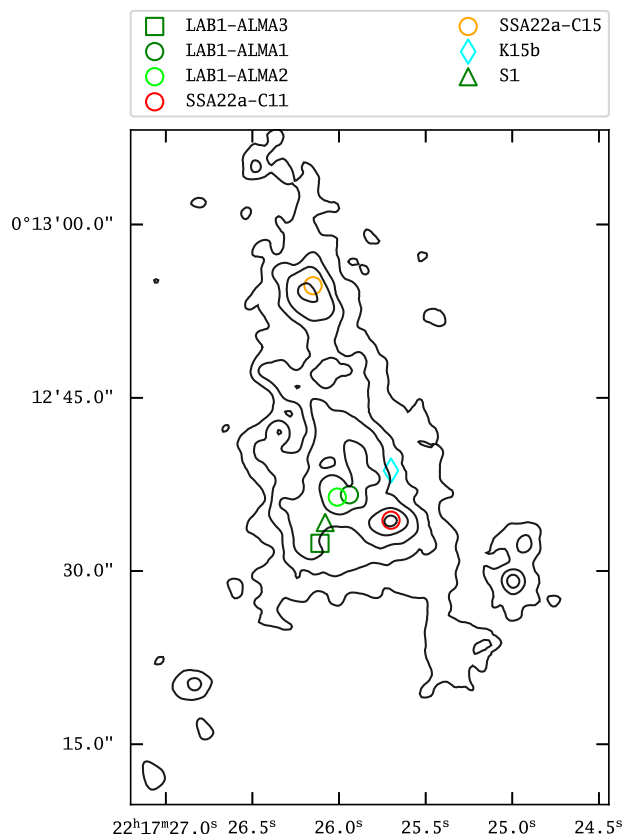


Fig. 1. Positions of confirmed galaxies within LAB 1 (Table 1) and Ly α surface brightness contours from our MUSE adaptive narrow band image (see Sect. 5.2). The *red* and *orange* circle mark the Lyman Break Galaxies SSA22a-C11 and SSA22a-C15 from Steidel et al. (2003), respectively. The *green* and *lime* circle mark the ALMA $850 \mu\text{m}$ detections LAB1-ALMA1 and LAB1-ALMA2 (Geach et al. 2016; Umemata et al. 2017), respectively. Centred between LAB1-ALMA1 and LAB1-ALMA2, and slightly offset ($\sim 1''$) to the south, is a VLA radio-continuum detection ($S_{10\text{cm}} = 7.3 \mu\text{Jy}$), which Ao et al. (2017) associate with the sub-mm detected pair – thus and for clarity we do not indicate this as a separate source (see Table 2 and Figure 4 in Ao et al. 2017). The *cyan diamond* indicates the K-band selected spectroscopically confirmed galaxy LAB01-K15b from Kubo et al. (2015, 2016), that has no sub-mm detected counterpart. The *green square* marks the ALMA $850 \mu\text{m}$ plus [C II] $158 \mu\text{m}$ detected source (Geach et al. 2016; Umemata et al. 2017). This source is also detected at 3 GHz with the VLA ($S_{10\text{cm}} = 7.3 \mu\text{Jy}$) and it has a tentative X-Ray counterpart (Ao et al. 2017) seen in the deep Chandra data from Lehmer et al. (2009a). The serendipitously found $z = 3.1$ [O III] emitter S1 from Geach et al. (2016) is marked with a *green triangle*. The symbols used to indicate the embedded galaxies within the blob will be used throughout the paper. North is to the top and west is to the left, and the axis indicate the coordinates in Right Ascension and Declination. The contours correspond surface-brightness levels $\text{SB}_{\text{Ly}\alpha} = [200, 100, 50, 25, 8.75] \times 10^{-19} \text{ erg s}^{-1} \text{ cm}^{-2} \text{ arcsec}^{-2}$. The morphological features apparent in those surface brightness contours will be discussed in detail in this paper.

while SSA22a-C15 is found close to the Ly α photometric centre of LAB 8. Both galaxies have their redshift confirmed via near-IR detections of their [O III] $\lambda\lambda 4963, 5007$ lines (McLinden

Steidel et al. (2003) tied their astrometry the HST guide star catalogue. Earlier versions of the HST guide star catalogue were known to contain systematic errors of up to $\sim 1''$ (Morrison et al. 2001). We thus may speculate that this is the reason for the coordinate offsets. Here we revise the coordinates of SSA22a-C11 and SSA22a-C15 according to our adopted reference frame (Table 1).

Table 1. Known sources within the Ly α blob

Name	RA	Dec	z	Refs.
SSA22a-C11	22 ^h 17 ^m 25.70 ^s	+00° 12' 34.4''	3.0999±0.0004	(1),(2)
SSA22a-C15	22 ^h 17 ^m 26.15 ^s	+00° 12' 54.7''	3.0986±0.0003	(1),(2)
LAB1-ALMA1	22 ^h 17 ^m 25.94 ^s	+00° 12' 36.6''	...	(3)
LAB1-ALMA2	22 ^h 17 ^m 26.01 ^s	+00° 12' 36.4''	...	(3)
LAB1-ALMA3	22 ^h 17 ^m 26.11 ^s	+00° 12' 36.4''	3.0993±0.0004	(3)
LAB01-K15b	22 ^h 17 ^m 25.70 ^s	+00° 12' 38.7''	3.1007±0.0002	(4)
S1	22 ^h 17 ^m 26.08 ^s	+00° 12' 34.2''	3.0968	(4),(5)

References. (1) Steidel et al. (2003); (2) McLinden et al. (2013); (3) Ume-hata et al. (2017); (4) Kubo et al. (2016); (5) Geach et al. (2016)

Notes. Coordinates from Steidel et al. (2003) have been adjusted to the here used 2MASS astrometric reference frame.

et al. 2013). Interestingly, the systemic redshift determined from [O III] does not differ from the Ly α emission line. This is not commonly the case for high- z Ly α emitting galaxies where the Ly α line is typically found to be offset by $\gtrsim 200 \text{ km s}^{-1}$ with respect to the systemic redshift (e.g. Rakic et al. 2011; Chonis et al. 2013; Trainor et al. 2015). Since positive Ly α redshift offsets are usually interpreted as signs of outflowing expanding gas, McLinden et al. (2013) argue that C11 and C15 have no such prominent outflows. Moreover, C11 has an inferred star-formation rate of $\lesssim 10 \text{ M}_{\odot} \text{ yr}^{-1}$ (Steidel et al. 1998, 2003), thus falls short by more than a factor of ten in producing the required amount of ionising photons to power LAB 1.

Given the potential of obscured star-formation or AGN activity in the blob, it became naturally the target of several sub-mm and radio campaigns (Chapman et al. 2001, 2003; Geach et al. 2014, 2016; Ume-hata et al. 2017; Ao et al. 2017). Initial sub-mm observations of LAB 1 with SCUBA on the James Clarke Maxwell telescope revealed a strong ($\approx 20 \text{ mJy}$) $850 \mu\text{m}$ continuum-source at the position of the blob (Chapman et al. 2001). Chapman et al. (2003) also reported a tentative detection of cold-molecular gas in the centre of the blob as traced by CO(4-3) emission in data from the Owens Valley Millimetre Array. Qualitatively these observations were consistent with the picture that LAB 1 harbours a heavily obscured AGN. However, later observations targeting the $850 \mu\text{m}$ continuum and the CO(4-3) emission with the Sub-Millimetre Array (Matsuda et al. 2007) and the IRAM Plateau de Bure interferometer (Yang et al. 2012), respectively, provided non-detections at upper limits that were inconsistent with the initial detections. These observations challenged the picture of an enshrouded AGN in LAB 1's centre. Nevertheless, imaging-polarimetry with FORS2 on the VLT by Hayes et al. (2011) revealed that the radial polarisation profile, as well as the orientation of the polarisation vectors is consistent with predictions from Ly α radiative-transfer theory for a central powering source (Dijkstra & Loeb 2008). More recent spectro-polarimetry with FORS2 by Beck et al. (2016) appears consistent with this scenario, although the interpretation of spectro-polarimetric Ly α data is more complex (Lee & Ahn 1998). Especially different scattering geometries and kinematics are degenerate with respect to observable polarisation signal (Eide et al. 2018). Moreover, Trebitsch et al. (2016) challenged the interpretation of Hayes et al. (2011) by showing that the observed polarisation signal can be reproduced in a pure cooling-flow scenario.

Withstanding difficulties and ambiguities in interpreting Ly α observables from LAB 1, advances in sub-mm detector technology and collecting area ultimately lead to a detection of three highly dust-enshrouded star-forming galaxies within LAB 1

(Geach et al. 2014, 2016). Adopting the nomenclature of Ume-hata et al. (2017), these $850 \mu\text{m}$ detected systems are denoted LAB1-ALMA1 to LAB1-ALMA3, and we list their coordinates in Table 1. LAB1-ALMA1 and LAB1-ALMA2 are in close vicinity to each other. Both sources were previously treated by Geach et al. (2016) as a single source with $S_{850 \mu\text{m}} \approx 1 \text{ mJy}$. The discrepancy with respect to the initial SCUBA measurements by Chapman et al. (2001) is more than a factor of ten. This combined with the non-detection of such bright sub-mm emission in other follow-up campaigns (Matsuda et al. 2007; Yang et al. 2012) is likely a result of unknown calibration or other unaccounted observational artefacts within those early sub-mm datasets of the system (Geach et al. 2016). Ao et al. (2017) report a potential 3 GHz counterpart to both sources, which is offset by 1.1'' to the south of LAB1-ALMA1 and LAB1-ALMA 2 (see also Figure 4 in Ao et al. 2017). LAB1-ALMA3 is detected in [C II] $158 \mu\text{m}$ emission (Ume-hata et al. 2017) and spatial coincident with a VLA 3GHz source from Ao et al. (2017). Moreover, Ao et al. (2017) find a weak X-Ray signal at the position of this source in the deep (400 ks) Chandra full-band (0.5 - 8 keV) image from Lehmer et al. (2009a). This X-Ray source is, however, below the significance criterion adopted in the blind search by Lehmer et al. (2009a). The total measured $850 \mu\text{m}$ flux density from these three resolved ALMA sources in the blob is 1.7 mJy. This flux corresponds, under standard dust-heating assumptions, to star-formation rates of $\sim 150 \text{ M}_{\odot} \text{ yr}^{-1}$. Moreover, hints for an extended low-surface brightness dust-component which is not detected by ALMA are seen in the fact that the single-dish SCUBA-2 observations (Geach et al. 2014) yield a factor of 2.7 higher flux compared to the interferometric measurement. Interestingly, the positions of LAB1-ALMA1 and LAB1-ALMA2 are at the centre of the circular pattern denoted by the polarisation vectors from Hayes et al. (2011). Thus the now converging results from sub-mm campaigns are corroborating the central engine hypothesis.

Further galaxy counterpart identifications were provided by Kubo et al. (2015, 2016) from near-infrared spectroscopic observations of K-Band selected galaxies with MOIRCS on the Subaru telescope. Their source LAB01-K15a is spatially coincident with the $850 \mu\text{m}$ and [C II] detected galaxy LAB1-ALMA3 and their source LAB01-K15c is coincident with the $850 \mu\text{m}$ detection LAB1-ALMA2. However, their source LAB01-K15b, confirmed via [O III] emission, is unique and we list its coordinates in Table 1. Moreover, Kubo et al. (2016) also report two fainter K-band selected galaxies whose photometric redshifts are consistent with them being members of the blob (see their Figure 2), but these galaxies have no spectroscopic redshifts. Lastly, Geach et al. (2016) found serendipitously an [O III] emitting galaxy at

$z = 3.1$ in their near-IR slit-spectrum of LAB 1. The coordinates of this source were presented by Umehata et al. (2017) and are reproduced in Table 1.

In summary, it is known that LAB 1 contains three dust-rich strongly star-forming systems (LAB1-ALMA1 to LAB1-ALMA3). These galaxies are accompanied by several less extreme star-forming systems, three of which have been detected (SSA22a-C11, K15b, and S1). Guided by the determined systemic redshifts of the galaxies associated with the blob (Table 1) we assume $z = 3.1$ as the systemic redshift of the blob throughout the remainder of this paper. To provide a visual overview of the confirmed galaxies within LAB 1 we plot their positions with respect to the Ly α surface brightness contours of the blob in Figure 1. For the latter we made already use of a result obtained from MUSE data discussed in the remainder of the paper (see Sect. 5.3 below). In such a dense environment further fainter satellite galaxies are expected (Geach et al. 2016). Given the combined star-formation rate of the embedded systems, the inferred ionising photon production rate is high-enough to power a substantial fraction of the blob's Ly α luminosity. Ly α polarisation measurements hint at a scenario, where scattering of Ly α photons emanating from the embedded sources is significantly contributing to the overall Ly α emissivity of the nebulae. However, the relative contribution of Ly α cooling radiation, either feedback or gravitationally driven, to the total Ly α photon budget is uncertain.

Previous IFS observations of LAB 1 were obtained with the SAURON instrument at the WHT (Bower et al. 2004; Weijmans et al. 2010). These observations revealed a complex morphokinematic structure of the system in Ly α . The identification of multiple clump-like features in these data was seen as evidence for the presence of multiple galaxies in the system, while the chaotic motions were interpreted as signs for galaxy-galaxy interactions. While these observations provided first insights into the complex structure of the system, they were limited in depth and spatial resolution. Here we will present the new deep MUSE observations of the system, that will allow us to map the spatial and kinematic structure of blob in unprecedented detail.

3. ESO VLT/MUSE Observations of LAB 1

LAB 1 was observed with MUSE (Bacon et al. 2010) in its wide field mode configuration without adaptive optics at the European Southern Observatories Unit Telescope 4 (Antu) in three service-mode programmes (094.A-0605 PI: M.Hayes, 095.A-0570 PI: Bower, and 097.A-0831 PI: Hayes) from 2014 to 2016. A log of these observations is given in Table 2. The individual exposure times are typically 1500 s, only with one exposure being significantly shorter (510 s). In total the three programmes accumulated a total open-shutter time of 63390 s (17.6 h) on the target.

The three different programmes centred the instrument on different regions of the blob. While programmes 094.A-0605 and 095.A-0570 centred the $1' \times 1'$ MUSE field of view slightly north of LAB 1 to encompass also the northern neighbouring Ly α blob LAB 8, programme 097.A-0831 centred on a region south-west of the brightest blob structure. This off-set was motivated by a detection of a previously unknown low-surface brightness extension of the blob in an reduction of the data from programme 094.A-0605 (see Geach et al. 2016). Each programme used the dithering and rotation pattern that is recommended in the the MUSE observing manual². This pattern reduces the systematic

Table 2. MUSE observations of LAB 1

Date-Time [yy/mm/dd-UT]	AM	DS ['']	SGS ['']	t_{exp} [s]	Sky	PID
14/11/13-00:33:06	1.14	0.61	0.69	1498	2	a [†]
14/11/13-00:59:29	1.19	0.82	0.73	1498	2	a
15/05/22-08:15:40	1.47	1.26	1.00	1500	3	b
15/05/22-08:42:34	1.34	0.94	0.94	1500	3	b
15/05/29-07:55:36	1.43	—	0.72	1500	3	b
15/05/29-08:22:31	1.31	0.59	0.71	1500	3	b
15/05/29-08:53:20	1.22	0.51	0.68	1500	3	b
15/05/29-09:20:15	1.16	0.54	0.65	1500	3	b
15/05/30-08:58:17	1.20	0.92	0.84	1500	3	b
15/05/30-09:25:11	1.15	0.67	0.82	1500	3	b
15/06/12-08:25:02	1.16	0.94	0.75	1500	2	b
15/06/12-08:51:58	1.13	1.21	0.78	1500	2	b [†]
15/06/12-09:21:56	1.11	1.06	0.79	1500	2	b
15/06/12-09:48:52	1.10	0.92	0.79	1500	2	b [†]
15/06/19-08:32:25	1.12	0.77	0.66	1498	2	a
15/06/19-08:59:09	1.10	0.80	0.68	1498	2	a [†]
15/06/19-09:37:28	1.11	0.88	0.63	1498	2	a
15/06/19-10:04:12	1.13	0.95	0.65	1498	2	a
15/06/20-07:40:02	1.19	0.78	0.70	1498	2	a
15/06/20-08:06:46	1.14	0.82	0.68	1498	2	a
15/06/20-08:38:08	1.11	0.93	0.66	1498	2	a
15/06/20-09:04:52	1.10	0.83	0.70	1498	2	a
15/06/22-08:01:52	1.14	1.14	0.63	1498	2	a [‡]
15/06/22-08:28:34	1.11	1.69	0.77	1498	2	a
15/06/24-06:39:13	1.32	0.60	0.68	1498	2	a
15/06/24-07:05:55	1.23	0.55	0.69	1498	2	a
15/09/17-02:35:33	1.12	1.10	0.71	1498	1	a
15/09/17-03:02:18	1.11	0.66	0.67	1498	1	a
16/07/15-09:09:06	1.23	1.10	1.14	1495	2	c
16/07/15-09:35:50	1.31	0.83	1.14	1495	2	c
16/08/12-06:47:59	1.16	1.12	0.89	1510	1	c
16/08/12-07:14:59	1.22	1.03	0.93	1510	1	c
16/09/02-02:33:13	1.22	0.84	1.00	1485	2	c
16/09/02-03:00:08	1.16	0.76	0.93	1485	2	c
16/09/05-01:57:24	1.29	0.87	1.00	1495	2	c
16/09/05-02:24:08	1.21	0.71	0.90	1495	2	c
16/09/25-00:19:41	1.36	0.91	1.01	1485	2	c
16/09/25-00:46:14	1.26	0.95	0.89	1485	2	c
16/09/30-00:11:15	1.32	1.76	1.02	1495	2	c
16/09/30-00:38:10	1.23	0.89	0.96	1495	2	c
16/10/04-00:43:00	1.18	1.56	1.39	510	2	c
16/10/04-01:55:53	1.10	0.85	1.02	1495	2	c
16/10/04-02:22:48	1.10	0.94	0.92	1495	2	c

Notes. AM = airmass, DS = Differential Image Motion Monitor Seeing measurement (FWHM), SGS = Slow Guiding System seeing measurement, Sky = sky transparency (1 = photometric, 2 = clear, 3 = thin cirrus), PID = ESO Programme ID (a = 094.A-0605, b = 095.A-0570, c = 097.A-0831, with [†] indicating an exposure affected by a continuum bright trail ($\sim 2''$ wide) and [‡] marking the exposure that could not be used due to a telescope tracking error).

effects that occur on the edges of the 24 individual spectrographs and their images slicers. Unfortunately, one exposure suffered from a severe tracking error and could not be used in the stack.

The DIMM seeing reported by ESO for the observation ranges from $0.5''$ to $1.7''$, but with the majority of exposures taken at sub-arcsecond seeing (mean: $0.87''$, median: $0.88''$). A potentially more accurate measurement of the seeing is provided

² <http://www.eso.org/sci/facilities/paranal/instruments/muse/doc.html>

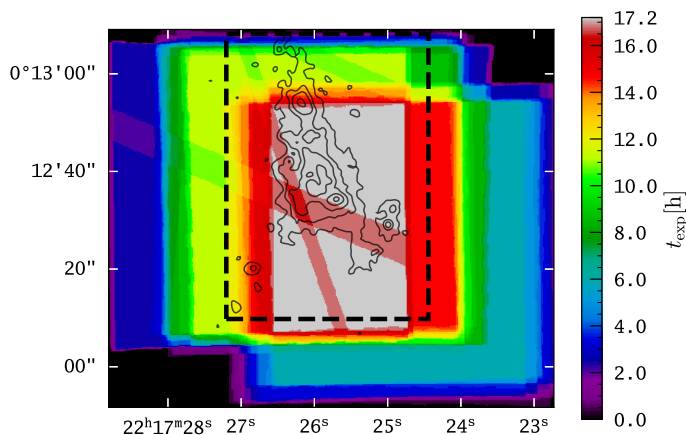


Fig. 2. Exposure map image for MUSE observations of LAB1 in the SSA22 field. The dashed rectangle indicates the zoomed-in region displayed in the spectral sequence shown in Figure 3. Diagonal bands of lower exposure times are a result of masked out regions in the final cube stack due to contamination by bright satellite tracks or meteor trails in the individual exposures. To indicate the position and morphology of LAB1 we also overlay the $\text{Ly}\alpha$ surface brightness contours from our MUSE adaptive narrow-band image (see Sect. 5.2).

by the FWHM measurements of stars in the meteorology fields recorded by MUSE’s slow-guiding system (SGS column of Table 2). Albeit having a slightly larger scatter, the measured image quality by the SGS is often a bit better than the site-wide values provided by the DIMM (mean: $0.83''$, median: $0.78''$),

Programmes 094.A-0605 and 097.A-0831 were taken without the blue cut-off filter in the fore-optics (extended wavelength mode), thus allowing the wavelength range from 465 nm to 930 nm to be sampled (although at the cost of second-order contaminations at $\lambda > 900$ nm), while programme 095.A-0570 was taken with the blue cut-off filter within the light path (nominal wavelength mode), thus sampling the wavelength range from 480 nm to 930 nm.

All observational raw data and the associated calibration frames were retrieved from the ESO Science Archive Facility³ using the raw-data query form. For all exposures the associated calibration frames (bias frames, arc lamp frames, continuum lamp frames, twilight flats, standard star exposures, and astrometric standard fields) were taken as part of the standard calibration plan for MUSE observations. This means especially, that twilight flats were taken typically once a week, while standard-star exposures are usually obtained daily. Nevertheless, some of the retrieved exposures were associated to standard star⁴ exposure that were taken one night before or after the science observations.

4. Data reduction

4.1. Production of the datacube

For the reduction of the 17.6 h of MUSE observations into a science-ready datacube we used version 2.4.2 of the MUSE Instrument Pipeline (MUSE DRS – Weilbacher et al. 2012,

2014) provided by ESO⁵ and version 3.0 of the MUSE Python Data Analysis Framework (MPDAF – Bacon et al. 2016; Piqueras et al. 2017) provided by the MUSE consortium⁶. The here utilised MUSE DRS version incorporates the so-called self-calibration procedure to improve the flat-fielding accuracy for deep datasets (Conseil et al. 2016). For our data reduction adopt the strategy that was employed to reduce the MUSE Hubble Ultra Deep Field (Bacon et al. 2017).

We first ran the MUSE DRS calibration recipes `muse_bias`, `muse_flat`, `muse_wavcal`, and `muse_lsf` on the calibration frames that are associated to each science and standard star exposure. We also used the `muse_twilight` recipe on the twilight frames. Next, we applied the resulting calibration data products to each science and standard star exposure using the recipe `muse_scibasic`. The resulting standard-star pixtables were then fed into `muse_standard` to create response curves. Those were then applied to each science exposure with the `muse_scipost` task, using its self-calibration feature, but not using its sky-subtraction capabilities.

In order for self-calibration to work optimally, regions containing sources that are bright in the continuum needed to be masked. While in principle the DRS can automatically detect such regions, we manually masked⁷ out bright continuum objects a bit more conservatively compared to the DRS generated mask. Additionally, four science exposures contained continuum bright linear trails from moving objects (likely satellite flares, meteors or airplanes – affected exposures are marked by a † in Table 2). These trails were also masked manually for the self-calibration.

We then removed night sky-emission with `muse_create_sky` and `muse_subtract_sky`. During this step we iteratively masked out regions that contained emission from the $\text{Ly}\alpha$ blob, so that this emission is not contaminating the subtracted night.

Next we resampled the individual sky-subtracted and flux-calibrated exposure tables to the final 3D grid with `muse_scipost_make_cube`. We defined this final grid via an initial run of `muse_expcombine` on a subset of pointings from each observing programme. Using MPDAF’s `combine` method we then produced an unweighted mean stack of those individual datacubes to produce the final science-ready datacube. Prior to this stack we masked out bright linear trails that were present in some observations (marked by a † in Table 2). We also ensured that remaining cosmic-ray residuals in the individual datacubes were filtered out in the final stack by using the κ - σ clipping algorithm in the `combine` task (2 maximum iterations with $\sigma_{\text{clip}} = 5$).

The resulting final datacube has 456×378 spatial elements (spaxels) that sample the sky parallel to right ascension and declination at $0.2'' \times 0.2''$. Each spaxel consists of 3802 spectral elements that sample the spectral domain from 4599.6 Å to 9350.8 Å linearly with steps of 1.25 Å.

Throughout the above procedure a formal variance propagation is also carried out by each of the employed routines, thus a second datacube containing the variance for each voxels is also produced. However, the resampling procedure in `muse_scipost_make_cube` produces correlated noise between

⁵ <https://www.eso.org/sci/software/pipelines/muse/muse-pipe-recipes.html>

⁶ <https://mpdaf.readthedocs.io/>

⁷ Manual masking was performed by visual inspection of the datacubes with the ds9 software (Joye & Mandel 2003) using polygon-shaped and circular regions. These regions were then converted into datacube masks using the `pyregion` python package.

³ <http://archive.eso.org/cms/eso-data.html>

⁴ The to our science observations associated spectrophotometric standards are Feige110, GJ754.1A, GD153, EG274, LTT3218, GD108, and LTT7987.

neighbouring volume pixels (see Figure 5 in Bacon et al. 2017). Since this co-variance term between neighbouring volume pixels (voxels) can not easily be accounted for in the final reduction, the formal variance cube contains underestimates of the true variances. By processing artificial pixtables filled only with Gaussian noise, Bacon et al. (2017) demonstrate that the variance for a voxel in an individual exposure datacube must be corrected by a factor of $(1/0.6)^2$ (see Figure 6 in Bacon et al. 2017). Following Bacon et al. (2017) we apply this correction to our final variance cube.

We display a map of the integration time for each spaxel in the MUSE datacube of LAB1 in Figure 2. The maximum integration time of 61920 s (17.2h) is reached in a $32'' \times 48''$ central region of our datacube. In this region all three ESO observing programmes overlap. This region completely encompassed the known extend of LAB 1 and LAB 8 prior to the here presented observations. Moreover, Figure 2 also illustrates the location of the masked out regions due to continuum-bright meteor trails or satellite tracks.

Lastly, we produce an emission line only datacube by subtracting a running median filter in spectral direction. This simple method for continuum removal has been proven effective in previous MUSE studies for isolating emission line signals (e.g. Borisova et al. 2016; Herenz & Wisotzki 2017; Herenz et al. 2017a,b; Arrigoni Battaia et al. 2019). Here we set the width of the median filter conservatively to 301 spectral layers (376.25 \AA).

4.2. Astrometric alignment

We register the MUSE datacube to an absolute astrometric frame by using the 2MASS point-source catalogue (Skrutskie et al. 2006). Unfortunately, there are only two 2MASS sources within the limited FoV of the MUSE and STIS observations, with one of those sources actually being an extended galaxy. We therefore use the only real 2MASS point source (2MASS J22172397+0012359) to anchor our astrometric reference frame in both observational datasets.

By tying the astrometric reference frame only to one source there remain in principle still several degrees of freedom with respect to geometrical distortions and rotation. However, rotational geometrical distortion are corrected for MUSE data at the pipeline level, and the accuracy of this procedure is constantly monitored by ESO using astrometric calibration fields.

We verified our absolute astrometry against an archival HST/STIS 50CCD clear-filter image that is partially overlapping with our MUSE data (Proposal ID: 9174, presented and analysed in Chapman et al. 2001, 2004). We tied the absolute astrometry of this image also to the 2MASS point source. By visual inspection via blinking in ds9 we then ensured that no offsets exist between both datasets. We conservatively estimate that the absolute astrometric accuracy of our data to be on the order of one MUSE pixel ($0.2''$).

5. Analysis and results

5.1. Velocity sliced Ly α emission maps

We present a spectral sequence of pseudo-narrowband images over the Ly α line in Figure 3. This sequence of images reveals the complex structure of the Ly α profile in different parts of the blob. A similar analysis was presented by Bower et al. (2004) based on 9 h deep SAURON IFS data. However, due to the limited depth of these observations, Bower et al. (2004) traced Ly α

emission only from -700 km s^{-1} to $+700 \text{ km s}^{-1}$. Spatial binning of deeper SAURON observations (23.5 h) hinted at the presence of extremely broad wings (Weijmans et al. 2010). The here presented data are significantly deeper than all previous observations and spatially resolves even fainter parts of the Ly α line wings. These wings appear to north and south in close proximity of the embedded sub-mm galaxies. Our observations reveal that here Ly α emission is apparent from $\sim -2500 \text{ km s}^{-1}$ to $+2500 \text{ km s}^{-1}$.

The most notable features discernible in the velocity slices through the Ly α emission shown in Figure 3 are:

1. A ring-like structure towards the north of the sub-mm sources. It is most clearly seen in the slice around 4979 \AA . In subsequent redder slices this “bubble” appears with less contrast. It appears as if its radius increases from $\sim 20 \text{ kpc}$ at 4979 \AA to up to $\sim 40 \text{ kpc}$ towards redder wavelengths.
2. A filamentary narrow bridge connecting LAB 1 to LAB 8 in the north. This bridge becomes visible in the slice at 4979 \AA and can be clearly followed until the 4989 \AA slice. For LAB 8 the flux shears from the north-west to the south-east with increasing wavelength, and this shearing of the Ly α emission in velocity space is also traced by the direction of the filament.
3. A faint extended, slightly curved, shell-like region towards the south-west of LAB 1. Along the major axis the extend of the shell is $\sim 120 \text{ kpc}$, and its projected thickness is $\sim 30 \text{ kpc}$. This low-surface brightness emission is visible in the slices from 4976.5 \AA to 4981.5 \AA . This previously undetected Ly α emitting region appears to be connected to the main area of LAB 1 via a low-surface brightness filament trailing from the north-east to the south-west. In the northern part of this shell-like region a compact high-surface brightness knot is visible.
4. A compact emission knot towards the north of LAB 8, that connects to LAB 8 via a faint low-surface brightness filament. This feature is seen in the slices at 4981.5 \AA and 4984 \AA . This newly discovered LAE and filament is close to the edge of the field of view of our observations, and thus only exposed at 8 h to 12 h, thus the noise in this part of the datacube is significantly larger. Nevertheless, as we will discuss in the following Sect. 5.4, the compact emitter is still a significant detection.
5. Another compact isolated Ly α line emitter towards the south-east of LAB 1 seen in the slices from 4984 \AA to 4989 \AA . We will show in the following Sect. 5.2, that this emitter is one of four newly detected compact Ly α emitters in close proximity towards the south-east of LAB 1.

A closer inspection of the velocity slices reveals that there appears to be an overall velocity shear. The bluer $v < 0 \text{ km s}^{-1}$ slices show predominantly emission towards the east, while the redder $v > 0 \text{ km s}^{-1}$ slices are dominated by emission from the west. This velocity shear will become more clear in our moment based analysis of the Ly α line profiles in Sect. 5.3 below.

5.2. S/N map and adaptive Ly α image

To visualise the overall Ly α surface-brightness morphology from LAB 1 from our MUSE datacube it would not be optimal to create a simple narrow-band image by summing over a certain number of datacube layers. Choosing a single bandwidth for such an image would either decrease the signal-to-noise ratio (S/N) for regions where the Ly α profiles are very broad if the bandwidth is chosen too small or, conversely, decrease the

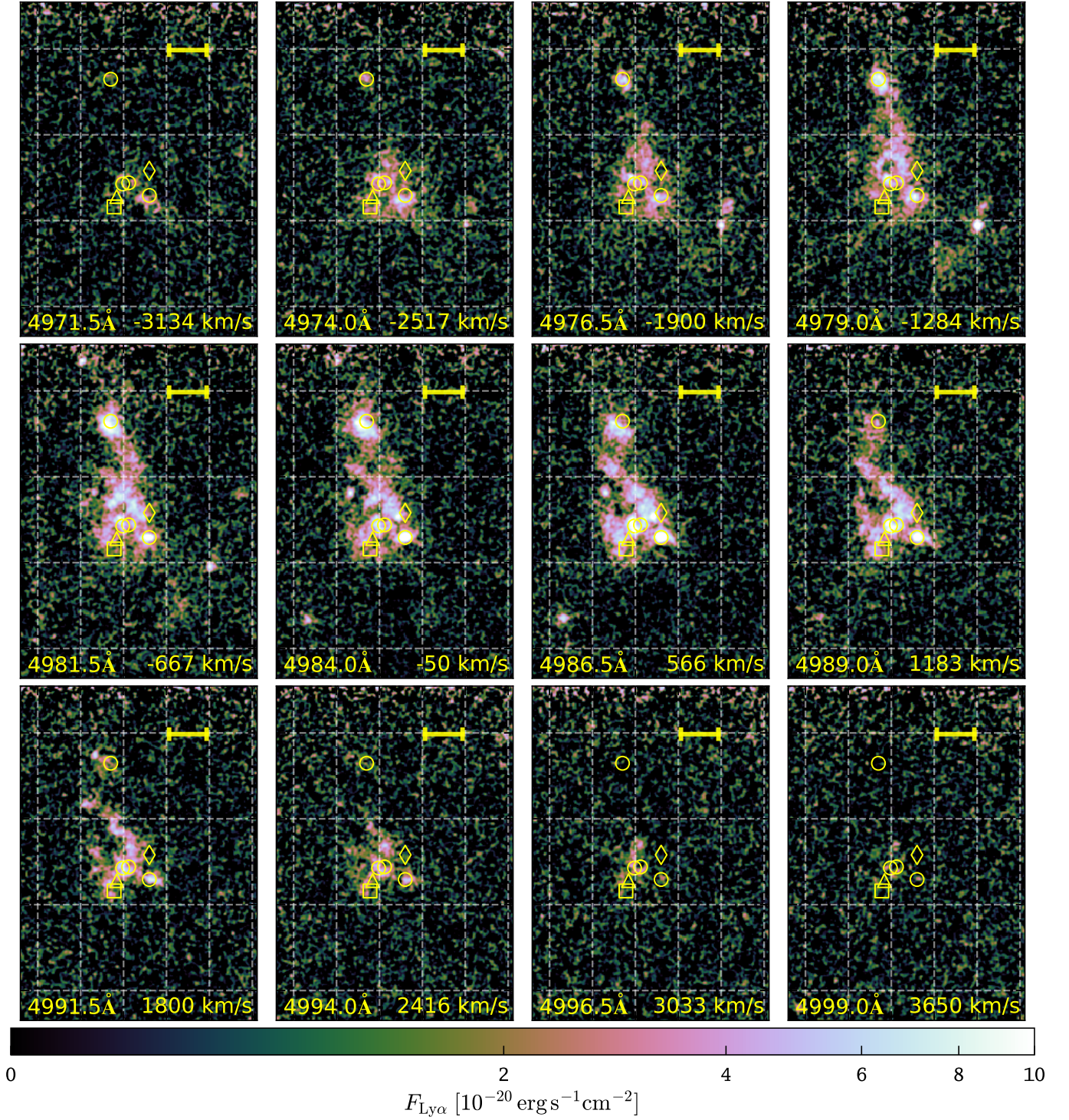


Fig. 3. Spectral sequence of pseudo-narrowband images of LAB 1 from 4971.5 Å to 4999.0 Å. Each image has a band-width of 2.5 Å. In order to enhance low-surface brightness features the images have been smoothed with a $\sigma = 1\text{px}$ (0.2'') Gaussian kernel. In each panel we indicate the positions of known galaxies within the blob (cf. Sect. 2 and Figure 1) and we also show a scale that indicates 50 kpc in projection at $z = 3.1$.

S/N in regions where Ly α is narrow if the bandwidth would optimally encompass the broader profiles. Furthermore, such a simple summation would also not account for the presence of velocity shear. We thus create an adaptive narrow-band image. For this image we sum only over voxels that contain Ly α flux. Our method is similar to the creation of the narrow-band images in the analysis of extended Ly α emission around QSOs

from MUSE data (e.g., Borisova et al. 2016; Arrigoni Battaia et al. 2019).

In order to find the spectral pixels over which we need to sum we utilised the 3D cross-correlation procedure of the LSDCat software⁸ (Herenz & Wisotzki 2017). LSDCat produces a S/N datacube by cross-correlating the continuum subtracted datacube

⁸ LSDCat is publicly available via the Astrophysics Source Code Library: <http://ascl.net/1612.002> (Herenz & Wisotzki 2016).

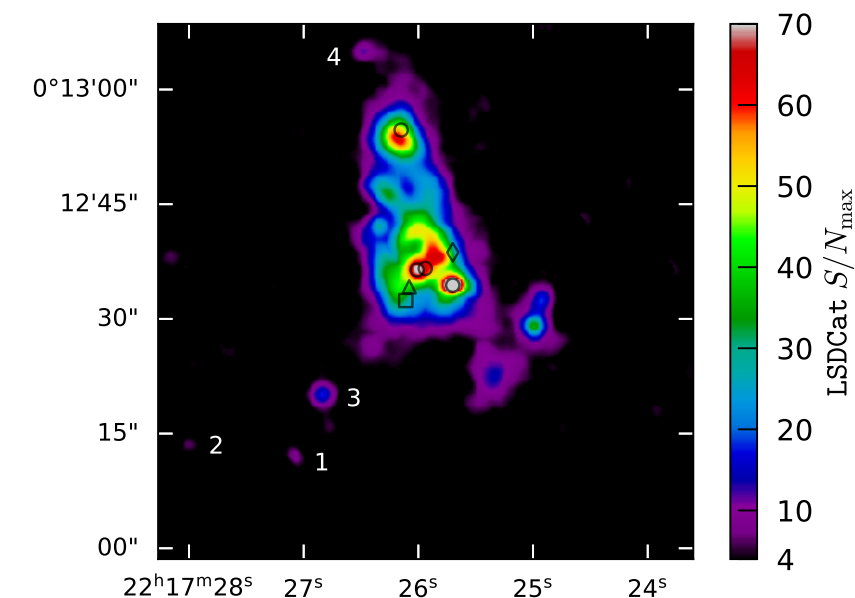


Fig. 4. Map of the maximum signal-to-noise ratio after cross-correlation with a 3D Gaussian template using the LSDCat software (Herenz & Wisotzki 2017). We show the maximum from the resulting S/N datacube between $\lambda_{\min} = 4962\text{\AA}$ and $\lambda_{\max} = 5005\text{\AA}$. The spatial FWHM of the utilised 3D Gaussian template was set $1.8''$, i.e. twice the seeing FWHM, while the spectral FWHM was set to 300 km s^{-1} . Foreground sources, where the continuum subtraction with a running median filter failed, are masked. Previously known galaxies at $z = 3.1$ are indicated using the in Figure 1. The four newly identified LAEs at $z = 3.1$ are labelled sequentially from 1 to 4 (see Section 5.4 and Table 3).

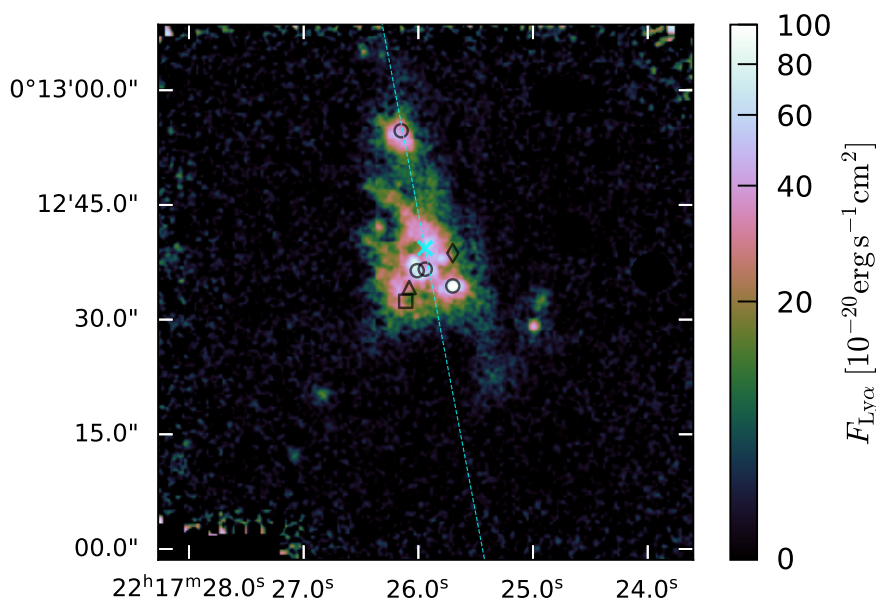


Fig. 5. Adaptive narrow-band image of LAB1. The image is the result of summing only over voxels in the continuum-subtracted datacube that have a $S/N > 4$ in the LSDCat cross-correlated datacube. For spaxels that do not contain voxels above this threshold we simply sum over 5\AA (four datacube layers) around $4985.6\text{\AA} (= (1 + z_{\text{LAB1}}) \times \lambda_{\text{Ly}\alpha})$. As in Figure 4, we masked sources where the continuum subtraction with a running median filter failed. In order to further enhance low-SB Ly α features, we smoothed the final image with a $\sigma = 0.2''$ Gaussian kernel. The photometric centre and the principal axis of the blob are indicated by a cyan cross and a cyan dashed line, respectively. Previously known galaxies at $z = 3.1$ are indicated using the same symbols as in Figure 1.

with a 3D Gaussian template. The tunable parameters of the template are the amount of spatial and spectral dispersion of the 3D Gaussian. Cross-correlation suppresses high-frequency noise while maximising the S/N of signals within the data that match the template. Hence, the method is commonly called “matched filtering” (see e.g., Vio & Andreani 2016; Zackay & Ofek 2017; Loomis et al. 2018). LSDCat was originally developed for the detection of Ly α emitting galaxies in blind MUSE surveys (see Herenz et al. 2017b and Urrutia et al. 2019). For this application the parameters of the template are optimally chosen when they match the width of the seeing point spread function (PSF) and the average line width of LAEs (see Sects. 4.2 and 4.3 in Herenz & Wisotzki 2017). We determine the width of the point spread function by fitting a 2D Gaussian profile to the bright star within our field of view in a 45\AA wide narrow-band image centred at $z_{\text{Ly}\alpha} = 3.1$. The so determined PSF full width at half maximum (FWHM) is $0.95''$ (4.75 MUSE spaxels). But, our goal here is not to optimise the template for compact emission line sources, but to maximise the S/N of faint low-surface brightness filaments in the outskirts of the blob. By experiment-

ing with different filter widths, we found that a spatial FWHM of roughly twice the seeing PSF FWHM (i.e. $1.8''$) optimally enhances the detectability of those structures while still preserving the morphology of small scale surface-brightness variations. Similarly, we varied the FWHM of the spectral part and found that 300 km/s is optimal for enhancing the detectability of the blobs low-surface brightness features.

In Figure 4 we show the resulting map when taking the maximum S/N in from the LSDCat S/N datacube around $z_{\text{Ly}\alpha} = 3.1$. This map clearly indicates that there exist several well defined high S/N peaks within the blob. The highest S/N peaks are found at the position of source C11, followed by a peak at the position LAB1-ALMA1. As a notable feature we find that the peak in the north corresponding to LAB 8 is spatially offset from the in LAB 8 embedded galaxy SSA22a-C15. Moreover, clear S/N peaks are seen in the shell in the south, as well as three from the blob isolated peaks in the east, and an almost isolated peak north of LAB 8. These isolated peaks, as well as the peak in the shell, represent newly identified Ly α emitters in close vicinity to the blob (see also the following Sect. 5.4). Our maximum S/N

map also accentuates the filamentary features that form a bridge between LAB 1 and LAB 8.

Equipped with the S/N datacube from LSDCat we constructed the optimal 3D extraction mask for our adaptive narrow-band image. We do so by summing the flux datacube in the spectral direction only over voxels that contain at least a S/N value above 4 in the S/N datacube. Spaxels that do not contain any S/N voxels above this threshold were summed over 4 spectral bins centred around 4983.4 Å (i.e. the wavelength of Ly α at $z = 3.1$). Therefore this image also includes a visual representation of the background noise in the source free region. The so constructed image is displayed in Figure 5.

The adaptive narrow-band image reveals more clearly several of the features that were already pointed out in the description of the velocity slices through the Ly α emission from the blob (Sect. 5.1). The region of the highest surface-brightness is directly coincident with the position of the Lyman break galaxy SSA22a-C11. Another region of high surface-brightness is found close to the position of the sub-mm detected galaxy pair LAB1-ALMA1 and LAB1-ALMA2. Notably, towards the north- and south- of this pair the Ly α flux is lower compared to the surrounding regions. The northern depression in flux corresponds to the ring-like structure seen in the velocity slices. Further in the north-east from this ring-like depression two filamentary structures emerge, with the southern one bounding close to a compact peak in emission. Interestingly, the sub-mm source LAB1-ALMA3, which is also detected in [C II] and radio emission (and potentially X-Ray, cf. Sect. 2), does not correspond to a peak of high-surface brightness, and neither does the [O III] detected galaxy S1 or the K-Band selected system LAB01-K15b. A faint diffuse bridge is connecting LAB 1 and LAB 8. Moreover, the galaxy SSA22a-C15 is offset from the peak in Ly α surface brightness. Towards the north of LAB 8 a narrow low-intensity filament seemingly connects to our newly identified LAE 4 (see Sect. 5.4 below). In the south-west of LAB 1 we clearly see a filament pointing from the main region of the blob to the newly detected shell-like ring. This shell-like ring is fragmented into two distinct regions, with the northern fragment consisting of a bright compact source and a fainter northern neighbour. Both sources have also corresponding distinct peaks in the S/N map. The southern fragment of the shell appears more diffuse and it does not show such a distinct peak. Finally, we also see in this image the isolated LAEs 1, 2, and 3 located towards the south-east of the blob (see Sect. 5.4 below). Intriguingly, the base of a potential low-surface brightness filament from the blob points into this direction.

We apply the formalism of image moments (e.g. Hu 1962; Stobie 1980, 1986) to the adaptive narrow-band image to calculate the photometric centre as well as the angle of the principal axis, θ_{PA} , of the LAB. In pixel-coordinates (x, y) of the adaptive narrow-band image I_{xy} the photometric centre (\bar{x}, \bar{y}) is defined as

$$(\bar{x}, \bar{y}) = \left(\frac{\sum_{xy} I_{xy} x}{\sum_{xy} I_{xy}}, \frac{\sum_{xy} I_{xy} y}{\sum_{xy} I_{xy}} \right), \quad (1)$$

and the angle of the principal axis is defined as

$$\theta_{PA} = \frac{1}{2} \arctan \left(\frac{2 \bar{x} \bar{y}}{\bar{x}^2 - \bar{y}^2} \right) + \frac{\pi}{2}, \quad (2)$$

with

$$(\bar{x}^2, \bar{y}^2) = \left(\frac{\sum_{xy} I_{xy} x^2}{\sum_{xy} I_{xy}} - \bar{x}^2, \frac{\sum_{xy} I_{xy} y^2}{\sum_{xy} I_{xy}} - \bar{y}^2 \right), \quad (3)$$

and

$$\overline{xy} = \frac{\sum_{xy} I_{xy} xy}{\sum_{xy} I_{xy}} - \bar{x} \bar{y}. \quad (4)$$

For these calculations we only considered pixels in the narrow-band image I_{xy} that have a corresponding pixel above a S/N of six in the maximum S/N map. Moreover, the definition of the angle of the principal axis in Eq. (2) is such that 0° corresponds to the axis from E to W, and that the angle increases counterclockwise to the north. The so obtained photometric centre converted to world coordinates is located at RA=22^h17^m25.94^s, Dec=+00°12'39.338", and for the angle of the principal axis we find $\theta_{PA} = 110.9^\circ$ north of east.

We show the position of the photometric centre in Figure 5 by a cyan cross. As can be seen, the photometric centre is located slightly eastwards to the ring-like flux depression. We also indicate the principal axis in Figure 5 by a dashed cyan line. Figuratively speaking, the principal axis is the axis along which the blob appears most elongated. Formally, it describes axis along which the variance in flux is maximised. For a light distribution of elliptical shape, the so defined principal axis would be oriented along the major axis of the ellipse. Thus our θ_{PA} measurement is comparable to the measurements of LAB position angles via ellipse fitting in Erb et al. (2011). We discuss the alignment between principal axis and gas kinematics in Sect. 6.3.1.

5.3. Moment based maps of the Ly α line profile

By visually inspecting the Ly α spectral profile as a function of position with the QFitsView software⁹ (Davies et al. 2010; Ott 2012), we find that the line profile complexity varies strongly throughout the blob. We illustrate this by showing a selection of representative profiles in Figure 6. As can be seen, in some region the profiles appear very broad and single peaked (e.g. panel 12 in Figure 6), while other regions are characterised by clearly double- (e.g. panel 1) or even multiply peaked Ly α lines (e.g. panel 3 or panel 10). The isolated LAEs in the outskirts (example in panel 4, see also Figure 9), or in the shell-like region (panel 7) show narrow single-peaked asymmetric Ly α profiles.

The varying complexity of the Ly α profiles as a function of position prohibit parametric fits of a simple model to the spaxels of the datacube in order to create maps of, e.g., the velocity centroid (v_r) or line-width (velocity dispersion σ_v). Such an analysis was presented for the much shallower SAURON data of LAB 1 (Bower et al. 2004; Weijmans et al. 2010), but the increased sensitivity and resolution of our MUSE data warrant a different approach. We thus resort on a moment-based non-parametric analysis.

For this analysis we first created maps of the central flux-weighted moment (1st moment)

$$m_1^{xy} = \frac{\sum_z z F_{xyz}}{\sum_z F_{xyz}}, \quad (5)$$

as well as maps of k -th flux-weighted moments

$$m_k^{xy} = \frac{\sum_z (z - m_1^{xy})^k F_{xyz}}{\sum_z F_{xyz}} \quad (6)$$

for $k = 2$, $k = 3$ and $k = 4$. In Eqs. (5) and (6), as well as in the following equations below, x and y denote the indices of

⁹ The QFitsView software is publicly available via the Astrophysics Source Code Library: <http://ascl.net/1210.019>.

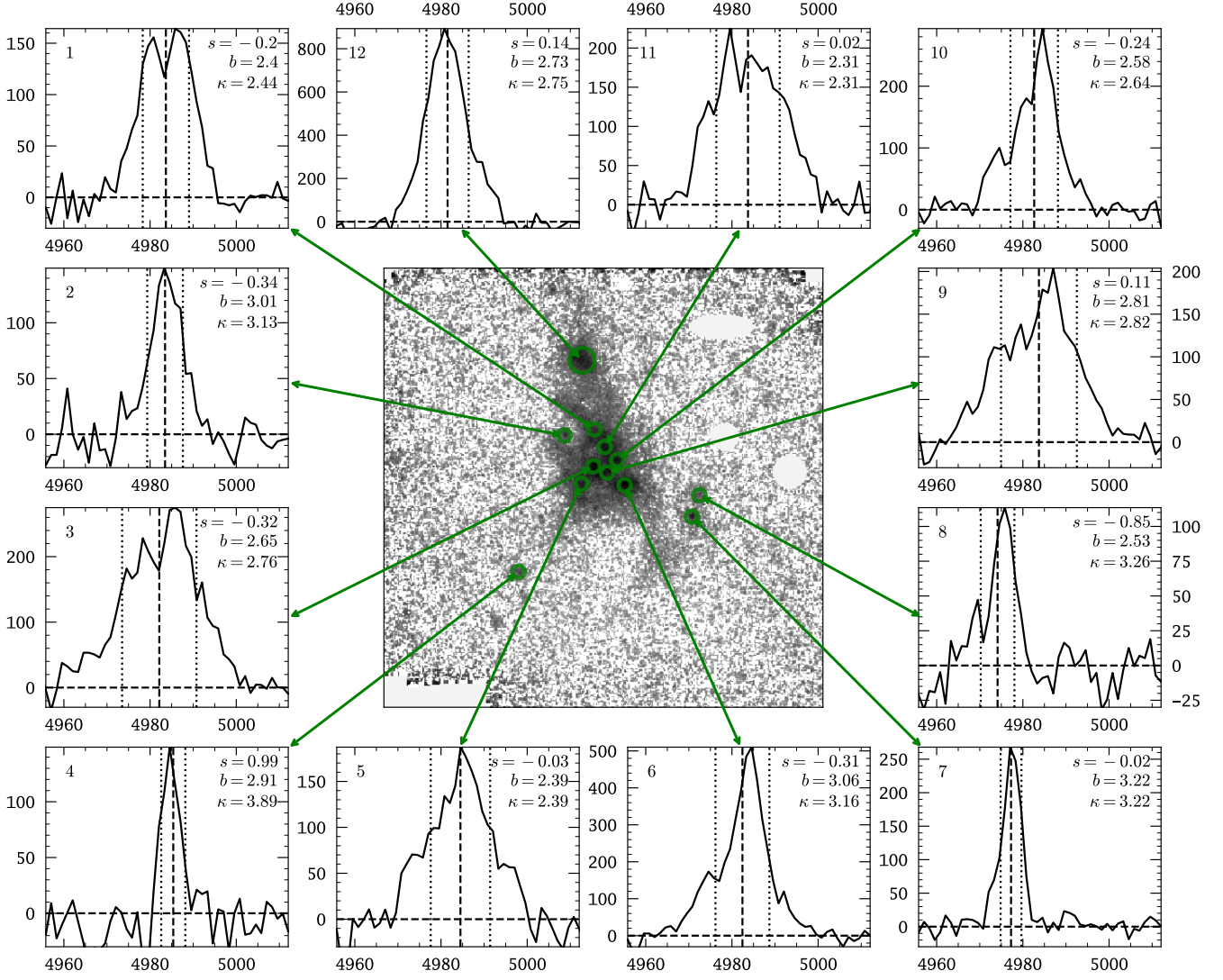


Fig. 6. Examples of the variety and complexity of the Ly α line profiles encountered in LAB 1. All profiles are extracted in circular apertures of 2'' diameter, except for LAB 8 where a 4'' diameter aperture was used. The image in the centre is the adaptive narrow-band image shown in Figure 5, but shown here in a logarithmic scale. Green circles represent the extraction apertures with lines connecting to the individual panels that display the profiles. For each profile the wavelength axis (in Å) is fixed, but the axis displaying the intensity (in $\text{erg s}^{-1} \text{cm}^{-2} \text{Å}^{-1}$) is scaled to encompass the maximum flux value of each profile. We also indicate in each panel the flux-weighted central moment (Eq. 5, dashed line), and the from the second flux-weighted moment obtained non-parametric measure for the width of the line (Eq. 6 with $k = 2$, dotted lines). Moreover, we display in the upper right corner of each panel the non-parametric descriptive measures skewness s (Eq. 8), kurtosis κ (Eq. 9), and bi-modality b (Eq. 10). All non-parametric descriptive statistics are computed by considering only the range of connected positive spectral bins blue- and red-wards of the peak.

spatial axes of the flux datacube F , while z indexes the spectral direction.

When using above equations, we have to ensure that the derived measurements (see below) are formally only valid if positive F values are considered. This is especially challenging in low-surface brightness regions of the blob. A possible approach would be to use an adaptive spatial binning scheme such as Voronoi-tessellation (e.g. Cappellari & Copin 2003), with the additional constraint of considering in each spatial bin only the range of positive spectral bins around the peak. However, as Voronoi-binning relies only on S/N to determine the bin-sizes and shapes, the resulting bins may average over rapidly varying features of the spectral profile. We thus do not spatially bin the datacube, instead we preserve as much of the spatial sampling by simply smoothing each datacube layer with a circular 2D Gaussian. The free parameter in this step is the smoothing-

kernel σ , and we will motivate its choice below. We moreover have to ensure that the majority of values contributing to the sums in Eqs. (5) and (6) are positive. For this purpose we use a 3D mask based on thresholding the LSDCat S/N datacube, in complete analogy to the 3D S/N mask used for the creation of the adaptive narrow-band image (Sect. 5.2). We call this S/N threshold “analysis threshold”. We found an optimal analysis threshold by visual inspection of the spatially smoothed datacube to ensure that the negative voxels are masked while simultaneously ensuring that the full line profiles contribute to the analysis. The optimal choice of the analysis threshold depends on the smoothing-kernel σ . We chose σ to be 0.8'', i.e. a bit smaller than the σ of the seeing PSF. This value significantly improved the S/N ratio of the Ly α profiles in the filaments and low surface-brightness regions of the blob, but only marginally decreases the spatial resolution. Thus, given that we characterised point-spread function

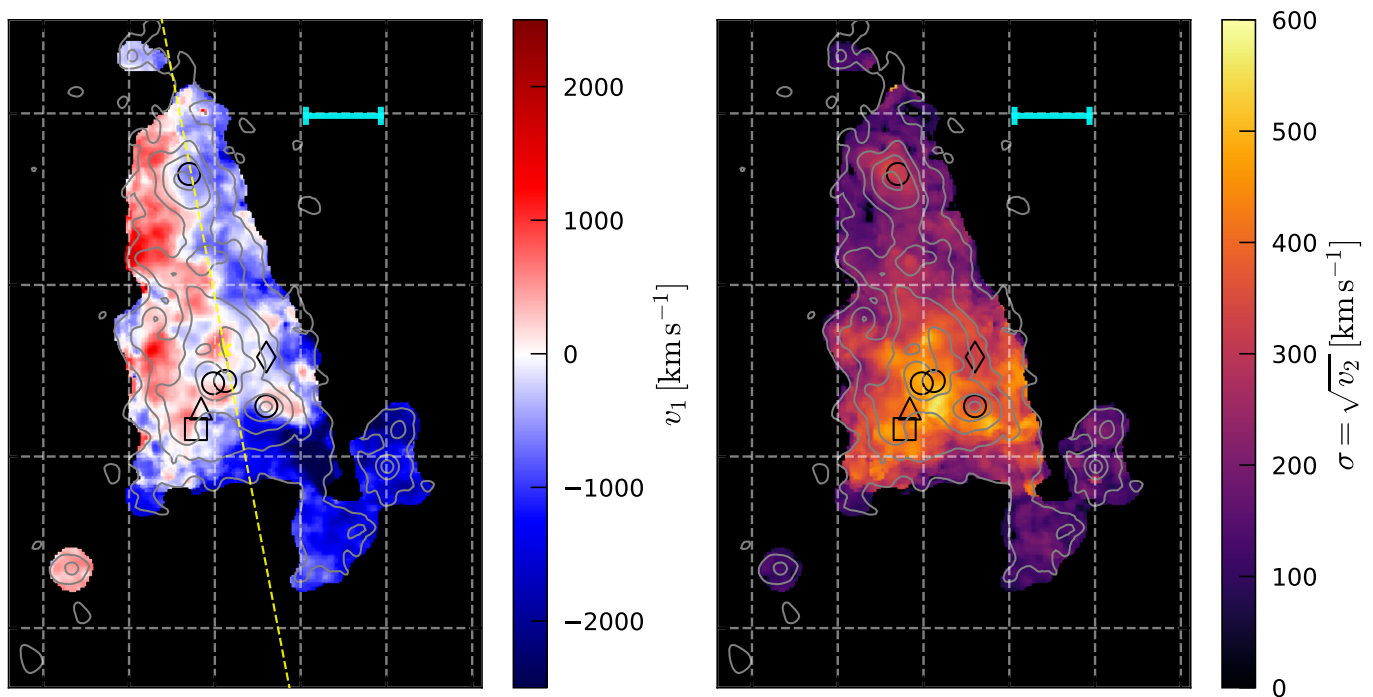


Fig. 7. Apparent line of sight-velocity (*left panel*) and apparent velocity dispersion (*right panel*) as measured from Ly α using the first and second flux weighted moments (Eq. 5 and 6 for $k = 2$). Before the moment-based analysis was carried out, each layer of the datacube was spatially smoothed with a $\sigma = 0.8''$ Gaussian kernel. In each spaxel only spectral bins above a S/N threshold of 4 in the LSDCat S/N datacube were used in the summations in Eq. (5) and Eq. (6). Moreover, the displayed map shows only spaxels that have a maximum S/N > 6. Thin grey contours indicate surface-brightness levels $\text{SB}_{\text{Ly}\alpha} = [200, 100, 50, 25, 8.75] \times 10^{-19} \text{ erg s}^{-1} \text{ cm}^{-2} \text{ arcsec}^{-2}$ as measured in the adaptive narrow-band image (Figure 5). The positions of confirmed galaxies within the blob are indicated with the same symbols as in Figure 1. The photometric centre and the principal axis of the blob (see Sect. 5.2 and Figure 5) are indicated by a yellow cross and a yellow dashed line, respectively. The horizontal cyan line in the upper right of each panel indicates a projected proper distance of 50 kpc.

blur in the MUSE observations of the blob by a 2D Gaussian of $\text{FWHM} = 0.95''$ (Sect. 5.2), the Gaussian blur of the maps from the moment based analysis is $0.9''$. For the smoothing-kernel with $\sigma = 0.8''$ the above mentioned constraints for the analysis threshold were fulfilled when masking out voxels below an LSDCat S/N of 4. Lastly, we employed a 2D mask by thresholding the maximum S/N map shown in Figure 4 to exclude spaxels where only a very small number of spectral bins would contribute to the resulting moments. Setting this display threshold as $\text{S/N}_{\text{max}} = 6$ efficiently removed such spaxels from the final moment based maps. However, as we will discuss below, for the maps that include the fourth moment we needed to increase the display threshold to $\text{S/N}_{\text{max}} = 15$ in order to avoid low-S/N biases in those maps.

The first moment map resulting from Eq. (5) directly translates into a line-of-sight velocity map. For this translation we fix the systemic redshift of LAB 1 to $z = 3.1$, in agreement with known redshifts of the galaxies within the blob. The so created v_r^{xy} map is shown in the left panel of Figure 7. There we also show the photometric centre and the principal axis that were computed from the adaptive narrow band image as described in the previous section. We point out that the principal axis is oriented orthogonal to the direction of the apparent large scale velocity gradient. This feature will be further discussed in Sect. 6.3.

By taking the square root of second moment map (Eq. 6, with $k = 2$) we compute a map that provides a measure of the width of the spectral profiles (right panel of Figure 7). We express the width of the profiles σ_v in km s^{-1} , but caution that this measurement can not be directly interpreted as velocity dispersion as it is often done for non-resonant emission lines. For ex-

ample, double- or multiple peaked profiles generally have larger second moments than single peaked profiles. Moreover, radiative transfer effects are also known to broaden the single-peaked Ly α line profiles when compared to non-resonant emission lines (see also Sect. 5.5). We thus call the second moment based measure “apparent velocity dispersion”. Lastly, the spectral resolution of MUSE also has an effect on the apparent velocity dispersion. Given the complexity of the profiles and the non-parametric nature of our measurement the effect of broadening the profiles via convolution with the spectrograph’s line spread function is not easily quantifiable. The measured instrumental width for MUSE at 4980\AA is $\sigma_{\text{inst}} \approx 75 \text{ km s}^{-1}$ (Bacon et al. 2017). As a figure of merit estimate, this translates into resolution corrections σ_{corr} of -34 km s^{-1} , -20 km s^{-1} , -15 km s^{-1} , and -10 km s^{-1} for apparent velocity dispersions of 100 km s^{-1} , 150 km s^{-1} , 200 km s^{-1} , and 300 km s^{-1} , respectively, if the observed line profiles and the line spread function are well approximated by a Gaussian profile i.e.

$$\sigma_{\text{corr}} = \sigma_v - \sqrt{\sigma_v^2 - \sigma_{\text{inst}}^2}. \quad (7)$$

Creating such moment-based maps of line-of-sight velocity and apparent velocity dispersion is common in the analysis of synthesized datacubes from radio-interferometric 21 cm observations of galaxies (e.g. Thompson et al. 2017, Section 10.5.4). It now is also routinely employed in the analyses of extended Ly α nebulae surrounding quasars (e.g. Borisova et al. 2016; Arrigoni Battaia et al. 2018, 2019; Drake et al. 2019). Moreover, recent theoretical work by Remolina-Gutiérrez & Forero-Romero (2019) and Smith et al. (2019) resort on a moment-based analysis in the analysis of Ly α profiles from Ly α radiative transfer simulations. However, in order to create maps that characterise the

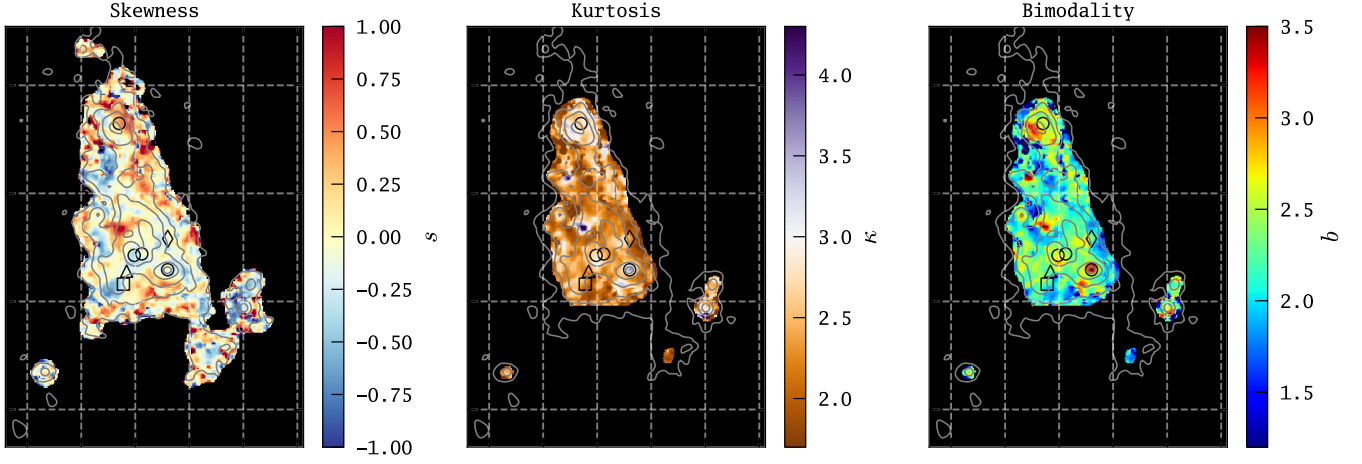


Fig. 8. Maps of higher-moment based non-parametric measurements visualise the varying complexity of the Ly α profiles morphologies as a function of position in the blob. We show maps of skewness s (left panel), kurtosis κ (centre panel) and bimodality b (right panel), as defined in Eq. (8), Eq. (9), and Eq. (10), respectively. Moreover, before applying these equations each layer of the datacube was smoothed with a $\sigma = 0.8''$ Gaussian kernel and for each spaxel only spectral bins above a S/N threshold of 4 in the LSDCat S/N datacube were used in the summations in Eq. (5) and Eq. (6). Moreover, the displayed map in the left panel (middle and right panel) shows only spaxels that have a maximum S/N > 6 (maximum S/N > 13). Skewness values $s = 0$ (yellow) indicate symmetric profiles, while $s < 0$ (shades of blue) indicates that the profile is asymmetric towards the blue and $s > 0$ (shades of red). Kurtosis values of $\kappa = 3$ (white) indicate that the wings of the profile are comparable to a Gaussian profile, while $\kappa > 3$ (shades of purple) indicate a larger tail extremity of the profiles (shades of brown). Bimodality b measures whether the profiles are double component ($b \lesssim 2.6$, green and blue colours) or single component ($b \gtrsim 3$, shown in red) profiles. However, given the presence of noise and finite spectral resolution a clear discriminatory power is not given by this measure in range $2.6 \lesssim b \lesssim 3$ (regions with yellow and orange colours). Contours and symbols are the same as in Figure 7.

varying complexity of the Ly α profile as a function of position in the blob, we use measurements involving the higher-moments. Remolina-Gutiérrez & Forero-Romero (2019) suggest to use the skewness s , the kurtosis κ , and the bimodality b . These measurements will be detailed in the following. To provide a visual guide on how to interpret these quantities we also display their values next to the example profiles from the blob shown in Figure 6.

We calculate a map of the Ly α profile skewness s via

$$s^{xy} = m_3^{xy} / (m_2^{xy})^{3/2}. \quad (8)$$

Skewness quantifies the asymmetry of the spectral profile. It is always $-1 \leq s \leq 1$. If $s \approx 0$ the profile has equal amounts of flux towards the red and blue side of the first central moment (e.g. panels 5, 7, and 11 in Figure 6), while for $s > 0$ more flux is redwards of m_1 (e.g. panels 4 and 12 in Figure 6) and for $s < 0$ more flux is bluewards of m_1 (e.g. panels 6, 8, and 10 in Figure 6). We show our computed map for s^{xy} in the left panel of Figure 8. Shimasaku et al. (2006) quantified the observed skewness in spectral profiles from Lyman α emitting galaxies by multiplying the definition given in Eq. (8) with a measure of the width of the line, however, we prefer to not entangle those two quantities. Other authors (Mallery et al. 2012; U et al. 2015) quantified skewness s by fitting a skewed Gaussian profile. But this approach does not capture the complex Ly α spectral profiles seen here in LAB 1. Moreover, Childs & Stanway (2018) showed recently that the skewness values derived from fitting an asymmetric Gaussian do not accurately capture the true skewness of Ly α profiles in the presence of finite spectral resolution and background noise.

We obtain a map of the kurtosis of the Ly α profiles via

$$\kappa^{xy} = \frac{m_4^{xy}}{(m_2^{xy})^2} \geq 1. \quad (9)$$

Kurtosis quantifies how much flux is in the wings of the profiles, i.e. their tail extremity, in comparison to the wings of Gaussian

profile¹⁰. For $\kappa = 3$ the wings are comparable to the Gaussian profile, while profiles with $\kappa > 3$ show more pronounced wings (e.g. panels 4, 6 and 8 in Figure 6), while $\kappa < 3$ indicates the absence of pronounced wings (e.g. panels 1, 6, and 11 in Figure 6). Of course, only wings that are significantly above the noise can contribute to this statistic. As a corollary regions of low S/N are biased towards to low kurtosis values. We avoid these biases by increasing the display threshold to $S/N_{\max} = 15$. We show our so obtained map for κ^{xy} in the centre panel of Figure 8.

We attempt to map the bimodality of the Ly α line profiles using

$$b^{xy} = \kappa^{xy} - (s^{xy})^2 \geq 1. \quad (10)$$

This non-parametric bi-modality measurement has recently been introduced into the Ly α literature by Remolina-Gutiérrez & Forero-Romero (2019). It can be considered as an attempt to quantify whether the profile shows single- or multiple components. Small values of b indicate that the profile can be described by a double component profile, while larger values correspond to single-component profiles. We point out that this measure is not a formal statistical test for bimodality, but it can capture the visual appearance of the Ly α profile morphologies. We find that for $b \lesssim 2.6$ profiles appear mostly to have clearly distinct double component structures (e.g. panels 1 and 8 in Figure 6), while profiles with $b \gtrsim 3$ are single peaked (e.g. panels 4 and 8 in Figure 6), or have a subdominant second component that is already mainly contributing to the kurtosis (e.g. panels 7 and 2 in Figure 6). In the range $2.6 \lesssim b \lesssim 3$, however, the discriminatory power of b appears not very strong, and visual inspection of those profiles indicates a high complexity with possible multiple components or peaks (see e.g. panels 3 and 11 in Figure 6). Moreover, since in regions of low S/N κ is biased towards low

¹⁰ A common misconception about κ is, that it is a measure of “peakedness” (Westfall 2014).

Table 3. Newly detected faint $z = 3.1$ LAEs around LAB1.

ID	RA	Dec	R_{kron}	$\log F_{\text{Ly}\alpha}$	Δv	σ_v
1	22 ^h 17 ^m 27.08 ^s	0°12'12.2"	0.6"	-17.2	+3690	127
2	22 ^h 17 ^m 28.01 ^s	0°12'13.7"	0.7"	-17.1	-1445	94
3	22 ^h 17 ^m 26.83 ^s	0°12'20.1"	1.5"	-16.7	+804	222
4	22 ^h 17 ^m 26.48 ^s	0°13'05.0"	1.3"	-16.6	-275	105

Notes. $F_{\text{Ly}\alpha}$ is the Ly α line flux in $\text{erg s}^{-1}\text{cm}^{-2}$ measured within a $2.5 \times R_{\text{kron}}$ aperture on the adaptive narrow-band image, Δv is the velocity difference in km s^{-1} with respect to $z = 3.1$, and σ_v is the measured width of the line in km s^{-1} . Δv and σ_v have been computed using the first and second flux-weighted moments (see Sect. 5.3).

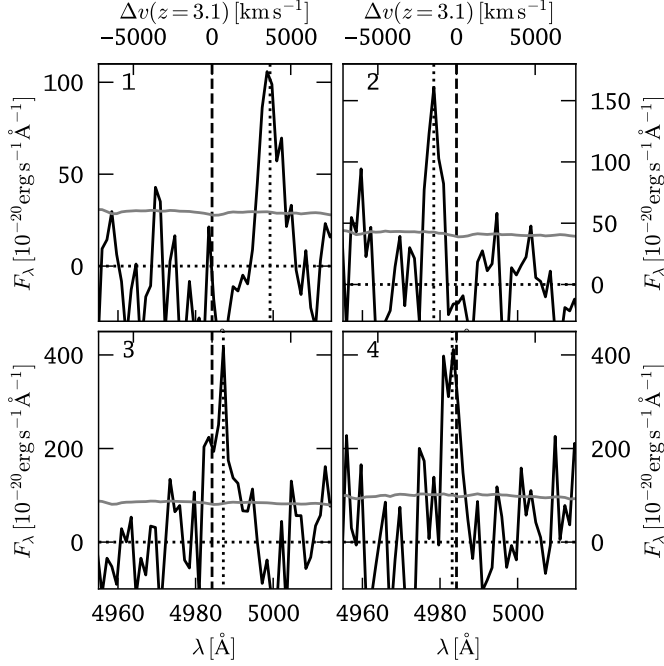


Fig. 9. Spectral profiles of the newly discovered LAEs 1 – 4 (as labelled in Figure 4, clockwise from top-left to bottom-right). Spectra (black lines) have been extracted within a circular aperture of radius R_{kron} (see Table 3). The propagated error spectrum from the variance cube in this aperture is shown as a grey line. The vertical dashed line indicates $z_{\text{Ly}\alpha} = 3.1$, whereas the vertical dotted lines indicate the measured redshifts from the profiles (see Table 3).

values, also b will be biased low in those regions. Thus, again we hide the biased regions by setting the display threshold to $S/N_{\text{max}} = 15$. We show our computed map for b^{xy} in the right panel of Figure 8.

We will describe and discuss the here derived and presented maps from the moment based analysis further in Sect. 6.3.

5.4. Newly discovered faint LAEs at $z \approx 3.1$ in proximity to LAB 1

As mentioned in Section 5.2, our S/N map revealed four detections that are not embedded in the extended Ly α radiation from the blob. We labelled those sources 1 – 4 in Figure 4. These sources are detected with $S/N > 6$ in the LSDCat cross-correlated datacube. Formally there exists one more detection with $S/N > 6$ at $z = 3.1$ close to the eastern border of Figure 4, however this detection turned out to be an artifact near the edge of our field of view.

The coordinates, Kron-radii, and fluxes of the newly detected LAEs are listed in Table 3. These measurements have been obtained with the LSDCat software (Herenz & Wisotzki 2017). In Figure 9 we show the spectral profiles of the detections. These 1D spectra have been extracted within a circular aperture of radius R_{kron} . No other lines are detected at these positions. Moreover, the line-profiles are reminiscent of the characteristic red-asymmetric line-profiles seen in LAEs (Yamada et al. 2012). Thus we are confident that the sources are LAEs in physical proximity to the blob. At $z = 3.1$ the range of the measured fluxes is $\log F_{\text{Ly}\alpha} [\text{erg s}^{-1}\text{cm}^{-2}] = -17.2 \dots -16.6$, which corresponds to Ly α luminosities $\log L_{\text{Ly}\alpha} [\text{erg s}^{-1}] = 41.7 \dots 42.3$. Hence those galaxies occupy the faint-end ($L_{\text{Ly}\alpha} < L_{\text{Ly}\alpha}^*$) of the LAE luminosity function (Drake et al. 2017a,b; Herenz et al. 2019) and are thus below the detection limit of classical narrow-band imaging surveys.

From the spectral profiles we measure the LAEs redshifts using the first flux-weighted moment (Eq. 5). The so obtained measurements are indicated as a vertical dotted lines in Figure 9. We list the velocity difference Δv with respect to $z = 3.1$ in Table 3. The two galaxies 1 and 3 south-east of the blob show large positive Δv . In fact, their redshifts appear to be a continuation of the overall west-to-east line-of-sight velocity gradient seen in the blob. For such large values of Δv radiative transfer effects are unlikely the main cause for the redshift offsets. We speculate, that the peculiar motion of those galaxies are driven by the gravitation potential of LAB 1's dark matter halo. The peculiar motion of the compact sources embedded in the northern part of the south-western shell-like structure could also be explained by this scenario. Moreover, the small blue-shift of our LAE 4 to the north of LAB 8 appears consistent with a smooth continuation of the overall blob velocity field. However, the base of the blobs filament which points towards the LAEs 1 and 3 shows blue-shifts and thus deviates from a smooth velocity-field continuation. As we will discuss in more detail in Sect. 6, such small scale modulations of a velocity field could be interpreted as filamentary cooling flows. Lastly, the eastern-most galaxy (2) is significantly blue-shifted and does not follow any trend. This galaxy might thus be at a larger distance from LAB 1's halo and thus not subject to its gravitational potential.

We quantify the line widths of the LAEs from the square root of the second flux-weighted moment (Eq. 6, with $k = 2$). The measured line widths σ_v for 3 out of 4 of the isolated LAEs are smaller than the typical observed widths throughout the blob, where $\sigma_v \gtrsim 180 \text{ km s}^{-1}$ (see Figure 7). As already discussed in Sect. 5.3, the moment-based σ_v measurement is not readily corrected for the instrumental resolution. Nevertheless, compared to the complexity of the line profiles seen in the blob, the profiles of the isolated LAEs appear relatively simple, hence the prescription for the figure-of-merit estimate in Eq. (7) provides a valid approximation here. The so corrected Ly α line-widths are 102 km s^{-1} , 57 km s^{-1} , 208 km s^{-1} , and 73 km s^{-1} for our LAEs 1, 2, 3, and 4, respectively. These line-widths are within the range of typical σ_v values obtained for a sample of brighter LAEs in the SSA22 field (Yamada et al. 2012, mean = 108 km s^{-1} , median = 84 km s^{-1}). We thus may consider these faint LAEs as an extension of the known SSA22 LAE population that exists below the detection limits of narrow-band selected samples. Moreover, Yamada et al. (2012) also found that the line-widths for some of the less extreme LABs in SSA22 are significantly broader than those of the isolated LAEs.

5.5. Detection of He II $\lambda 1640$ emission

We detect low-SB He II emission from three distinct regions within the Ly α blob. We visualise this detection in Figure 10, where we show a the resulting maximum S/N map from the LSDCat 3D cross-correlated datacube, as well as an adaptive narrow-band image (see Sect. 5.2). Here we evaluated the S/N datacube between $\lambda_{\min} = 6719\text{\AA}$ and $\lambda_{\max} = 6729\text{\AA}$ (i.e. $\pm 5\text{\AA}$ around He II at $z = 3.1$). Moreover, the adaptive narrowband was extracted by using voxels with $S/N > 3$ from the S/N datacube. In order to provide a visual representation of the noise level in regions not containing any signal, we summed spaxels with $S/N < 3$ by $\pm 2\text{\AA}$ around 6724\AA .

We label the three regions where He II is detected with $S/N > 6$ “south”, “north”, and “LAB8” in Figure 10. The “south” region is located south-west in close proximity the ALMA continuum sources LAB1-ALMA1 and LAB1-ALMA2 while being slightly north-east in vicinity of the Lyman break galaxy SSA22a-C11. The “north” He II region can not be associated with any known source in LAB 1. It is located in the north-western part of the circular Ly α flux depression described as “bubble” in Sects. 5.1 and 5.2. Lastly, the “LAB8” region appears in very close proximity to the Lyman break galaxy SSA22a-C15. We report in Table 4 positions of those three S/N-weighted positions of regions calculated following Eq. (21) of Herenz & Wisotzki (2017). All regions are within regions of Ly α surface-brightness above $5 \times 10^{-18} \text{erg s}^{-1} \text{cm}^{-2} \text{arcsec}^{-2}$. But the morphological features seen in He II are considerably different compared to the morphology of Ly α above this surface brightness limit.

In order to extract 1D spectra from those regions we created apertures consisting of contiguous regions with $S/N > 5.5$ in the maximum S/N image. The corresponding areas of these He II morphology-matched apertures are also listed in Table 4. In those regions extracted spectral profiles of the He II emission are shown in the bottom panels of Figure 10. We furthermore compare in this figure the He II spectral profiles to the Ly α profiles extracted in the same regions.

We measured the He II fluxes in those regions by summing the spectral profiles shown in Figure 10 over their full width at zero intensity. The error on the fluxes was obtained from 10^4 Monte-Carlo (MC) realisations of the profile, where we used the propagated variances as input for adding noise to each spectral bin. The so obtained flux measurements are listed in Table 4. Given the areas of the extraction apertures, the measured fluxes correspond to He II surface-brightness values of $7.6 \times 10^{-19} \text{erg s}^{-1} \text{cm}^{-2} \text{arcsec}^{-2}$, $5.7 \times 10^{-19} \text{erg s}^{-1} \text{cm}^{-2} \text{arcsec}^{-2}$, and $7.6 \times 10^{-19} \text{erg s}^{-1} \text{cm}^{-2} \text{arcsec}^{-2}$ for region “south”, “north”, and “LAB8”, respectively. The measured He II surface-brightness is $\sim 4 - 5$ times fainter than the upper limits reported for a previous attempt to detect He II emission in LAB 1 using narrow-band imaging (Arrigoni Battaia et al. 2015).

To quantify the He II/Ly α flux ratios we measured the Ly α fluxes over their full width at zero intensity within the three He II emitting regions. We obtained $F_{\text{Ly}\alpha} = 1.7 \times 10^{-16} \text{erg s}^{-1} \text{cm}^{-2}$, $1 \times 10^{-16} \text{erg s}^{-1} \text{cm}^{-2}$, and $6.1 \times 10^{-17} \text{erg s}^{-1} \text{cm}^{-2}$, corresponding to He II/Ly α 0.06 ± 0.01 , 0.07 ± 0.01 , and 0.10 ± 0.02 , for region “south”, “north”, and “LAB8”, respectively (see also Table 4). The errors on those ratios have been computed from 10^4 MC simulations for the individual He II and Ly α flux measurements. From the previous non-detection of He II Arrigoni Battaia et al. (2015) determined upper limits He II/Ly $\alpha < 0.11$ for LAB 1 and He II/Ly $\alpha < 0.22$ for LAB8, thus the measured He II/Ly α ratios are a factor of two lower.

Using the first flux-weighted moment (Eq. 5) on the extracted profiles, we determined the relative redshift offset between He II and the Ly α $\Delta v(z_{\text{Ly}\alpha}) = c \times (z_{\text{Ly}\alpha} - z_{\text{HeII}})/(1 + z_{\text{HeII}})$. Again, the errors have been computed from 10^4 MC realisations.

A significant offset between Ly α and He II is only detected for the LAB 8 region, where Ly α appears modestly blue-shifted. Blue-shifted Ly α emission with respect to non-resonant nebular lines is atypical for normal Ly α emitting galaxies, that show often $\Delta v(z_{\text{Ly}\alpha}) \gtrsim 200 \text{km s}^{-1}$ (e.g. Rakic et al. 2011; Song et al. 2014), although few exceptions exist (e.g. Trainor et al. 2015). Interestingly, our non-detections of velocity offsets between Ly α and He II around C11 and LAB 8 is consistent with the non-detection of offsets between Ly α and [O III] for those systems by McLinden et al. (2013). This hints at a physical connection between the He II emitting zones and the galaxies in their vicinity (see discussion in Sect. 6.4).

Lastly, it is visible in Figure 10 that in all three regions the Ly α profile appears broader compared to He II. To quantify this we measured the width of the He II and Ly α lines, σ_v^{HeII} and $\sigma_v^{\text{Ly}\alpha}$, using the second flux-weighted moment (Eq. 6, with $k = 2$). The so obtained measurements are reported in Table 4. We find that Ly α is $1.6\times$, $2.4\times$, and $1.4\times$ broader than He II in the “south”, “north” and “LAB8” region, respectively.

5.6. Non-detection of the C IV $\lambda\lambda 1548, 1550$ doublet

We detect no significant signal from the C IV doublet (1548.203\AA and 1550.777\AA) in the MUSE data of LAB 1. This can be seen in Figure 11 where we show the maximum S/N map for C IV from evaluation of the 3D cross-correlated S/N datacube (see Sect. 5.2). Here the S/N cube was evaluated between $\lambda_{\min} = 6345\text{\AA}$ and $\lambda_{\max} = 6360\text{\AA}$. While there are a few patches within the blob that indicate possible signal at $S/N \approx 5$, this spectral region of the datacube is highly contaminated by sky-subtraction residuals. As these systematic residuals are not captured in the variance datacube, the formal S/N estimates are biased high. These sky-subtraction residuals appear especially pronounced at the edges of the individual observational datasets (see exposure map in Figure 2). These edge-residuals are apparent as a patchy horizontal stripe of $S/N \approx 4$ values slightly south of the photometric centre of LAB 8, as well as a vertical stripe on the western edge of the displayed region. A few pixels in the maximum S/N map show values above 5 in regions within the blob, but the extracted spectra in those regions do not show signal. We show in Figure 11 the spectral region of interest for C IV for the spectra extracted within the three He II emitting regions (Sect. 5.5). In order to suppress the high-frequency sky-noise and residuals we also smoothed those spectra with a $\sigma = 3.6\text{\AA}$ wide Gaussian. Interestingly, the so smoothed spectrum (shown as a blue line in Figure 11) indeed appears to show a small bump at the position of the $\lambda 1549$ line in all three regions. However, from the noise in those three regions (shown as a grey line in Figure 11), it is obvious that these features are not significant and can be only considered as a hint of C IV emission.

To provide upper limits on C IV emission we perform a source insertion and recovery experiment. For this experiment we assume that the C IV emission would be co-spatial with the He II emitting regions. As noted in Sect. 5.5, each of the three He II emitting region is defined by a cluster of connected spaxels that have $S/N > 5.5$. For simplicity we assume constant surface brightness within each region. Furthermore, we model the spectral profile of the $\lambda\lambda 1548, 1550$ doublet by two Gaussians, where the dispersion is set to the average width mea-

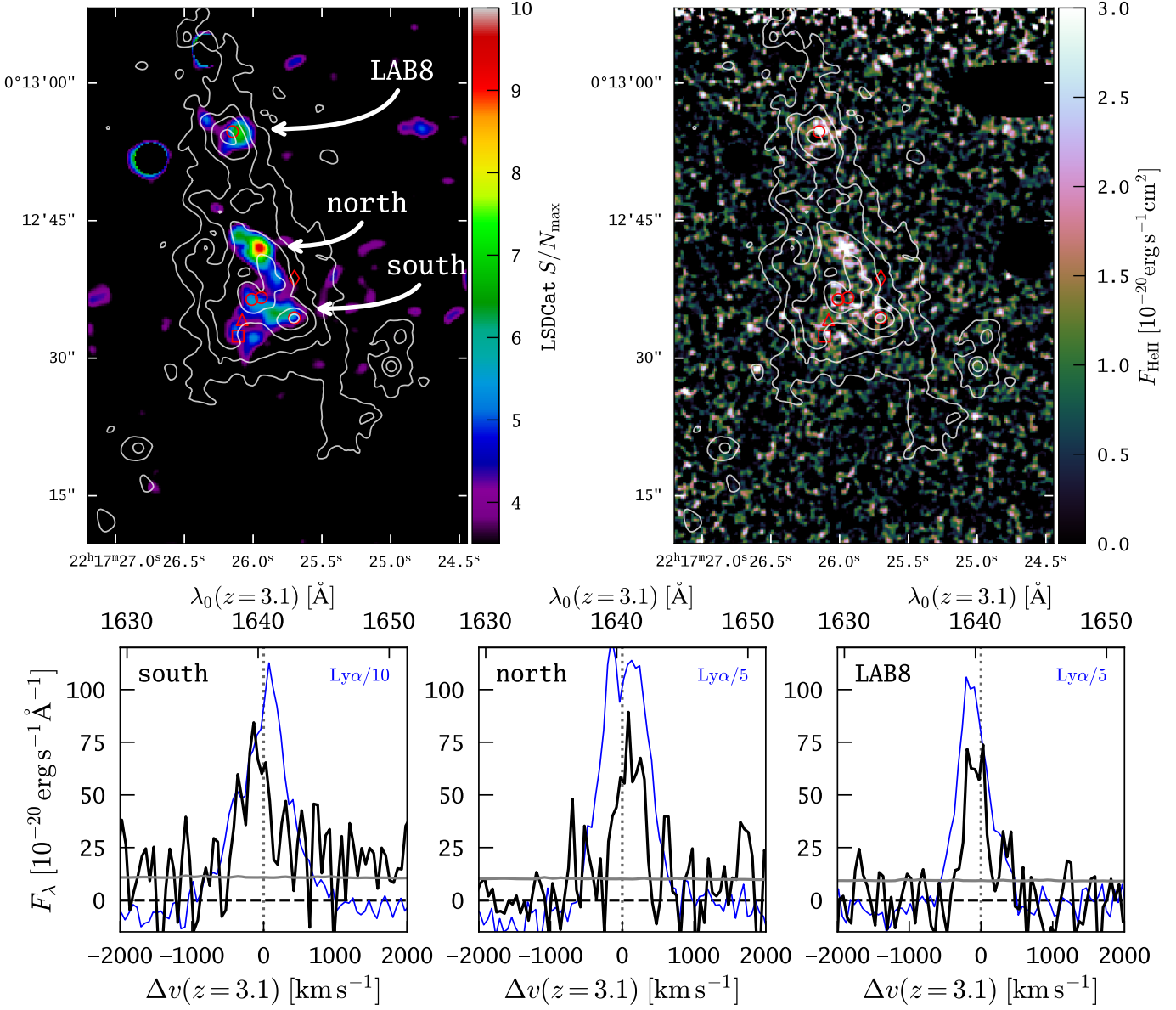


Fig. 10. Detection of extended He II $\lambda 1640$ fuzz in three distinct regions within LAB 1. *Top Left:* Map of the maximal He II S/N after cross-correlation with a 3D Gaussian template (see Sect. 5.2). We show the maximum from the S/N database between $\lambda_{\min} = 6719\text{\AA}$ and $\lambda_{\max} = 6729\text{\AA}$ (i.e. $\pm 5\text{\AA}$ around He II at $z = 3.1$). We label the three He II emitting regions “south”, “north”, and “LAB8” as indicated. *Top Right:* Adaptive He II narrow-band image. The creation of this image followed a similar procedure as for the adaptive Ly α narrow-band image (see Figure 5 and Sect. 5.2), except that here the used S/N analysis threshold is 3, and the default band-width for non-detections above this threshold is set to 3 databcube layers. The adaptive narrow-band image was additionally smoothed with a $\sigma = 1\text{px}$ ($0.2''$) Gaussian kernel. Grey contours indicate Ly α surface-brightness levels $\text{SB}_{\text{Ly}\alpha} = [200, 100, 50, 25, 8.75] \times 10^{-19} \text{ erg s}^{-1} \text{ cm}^{-2} \text{ arcsec}^{-2}$ as measured in the adaptive narrow-band image (Figure 5). In addition to the foreground galaxies in the west where bright continuum emission corroborated the median-filter subtraction continuum removal, we also masked out O III line emission from a $z = 0.3$ galaxy (at the northern edge of the image), and H β emission from a $z = 0.4$ galaxy (at the north-western edge of the image), as these highly significant emission line coincide with the $z = 3.1$ He II emission. *Bottom panels:* He II spectral profiles extracted from the three regions “south” (*bottom left panel*), “north” (*bottom centre panel*) and “LAB8” (*bottom right panel*). The black line is the spectrum and the grey line shows the propagated error from the variance cube. The bottom axis is given in velocities and the top axis indicates rest-frame wavelength, both for $z = 3.1$. The vertical dotted line indicates the rest-frame wavelength of He II (1640.42\AA). Extraction was performed by defining apertures connected regions of pixels above a S/N threshold of 6 in the maximum S/N map. For comparison we also show the Ly α profiles scaled by a factor of 10 (5) for the “south” (“north” and “LAB8”) regions as blue lines (for those profiles only the bottom velocity axis is relevant).

sured from the He II line: $\langle \sigma_v^{\text{HeII}} \rangle = 215 \text{ km s}^{-1}$ and we fix the ratio to 1.7 between $\lambda 1548$ and $\lambda 1550$. We implant the so generated C IV emitting regions at surface-brightness levels from $10^{-19} \text{ erg s}^{-1} \text{ cm}^{-2} \text{ arcsec}^{-2}$ to $9 \times 10^{-19} \text{ erg s}^{-1} \text{ cm}^{-2} \text{ arcsec}^{-2}$ in steps of $10^{-19} \text{ erg s}^{-1} \text{ cm}^{-2} \text{ arcsec}^{-2}$ prior to median-filter subtracting the fully reduced databcube. After median-filter sub-

tracting each databcube with artificial C IV sources we ran the 3D cross-correlation procedure from LSDCat. From this experiment we found that we would detect the C IV emission significantly in all three regions at surface-brightness levels $\geq 8 \times 10^{-19} \text{ erg s}^{-1} \text{ cm}^{-2} \text{ arcsec}^{-2}$. Given the areas of the three He II emitting regions, our surface-brightness limit corresponds

Table 4. Properties of He II $\lambda 1640$ emitting regions within the Ly α blob

Name	RA [J2000]	Dec [J2000]	Area □''	F_{HeII} [10^{-18} erg/s/cm 2]	$\Delta v(z_{\text{Ly}\alpha})$ [km/s]	$\sigma_{\text{v}}^{\text{HeII}}$ [km/s]	$\sigma_{\text{v}}^{\text{Ly}\alpha}$ [km/s]	He II/Ly α	C IV/Ly α
south	22 ^h 17 ^m 25.89 ^s	+00°12'35.3''	13.9	10.5±1.8	+13±68	289±55	464±9	0.06±0.01	≤ 0.06
north	22 ^h 17 ^m 26.01 ^s	+00°12'42.2''	12.6	7.2±1.1	−42±51	152±24	368±4	0.07±0.01	≤ 0.10
LAB8	22 ^h 17 ^m 26.12 ^s	+00°12'54.1''	8.8	6.7±0.9	−109±22	207±44	298±6	0.11±0.02	≤ 0.11

Notes. The area of the He II emitting regions is defined as the connected area of spaxels with S/N > 6 in the maximum S/N map (Figure 10). $\Delta v(z_{\text{Ly}\alpha})$ is the relative velocity offset between Ly α and He II emission: $\Delta v(z_{\text{Ly}\alpha}) = c \times (z_{\text{Ly}\alpha} - z_{\text{HeII}})/(1 + z_{\text{HeII}})$

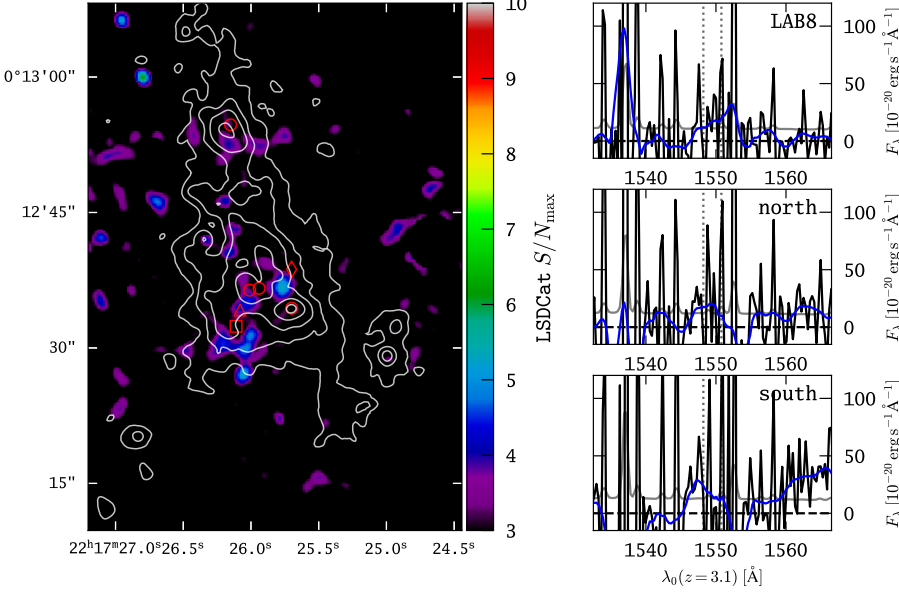


Fig. 11. Non-detection of significant signal from C IV emission within LAB 1. *Left panel:* Maximum S/N after cross-correlation with a 3D Gaussian template (see Sect. 5.2). Here the S/N cube was evaluated between $\lambda_{\text{min}} = 6345\text{\AA}$ and $\lambda_{\text{max}} = 6360\text{\AA}$. *Right panels:* Spectral extractions in the regions “south”, “north” and “LAB 8”, where significant He II emission was detected (Figure 10). In each of those panels the black curve shows the extracted spectrum, while the grey curve shows the propagated noise from the variance datacube. Vertical dotted lines indicate the rest-frame wavelengths of the C IV doublet. We also show a smoothed version (Gaussian window, $\sigma = 3$ px) of the spectrum (blue curve), which suppresses the high-frequency and high-amplitude oscillations from systematic sky-subtraction residuals in this wavelength range.

upper limits in C IV flux of $1.1 \times 10^{-16} \text{erg s}^{-1} \text{cm}^{-2}$, $1.0 \times 10^{-16} \text{erg s}^{-1} \text{cm}^{-2}$, and $6.1 \times 10^{-16} \text{erg s}^{-1} \text{cm}^{-2}$ for region “south”, “north”, and “LAB 8”, respectively. Given the measured Ly α fluxes in those regions (see Sect. 5.5), this corresponds to upper limits in C IV/Ly α ratios of 0.06, 0.1, and 0.11 for region “south”, “north”, and “LAB 8”, respectively. These limits on the ratios are a factor of ~ 2 lower than the ratios reported by Arrigoni Battaia et al. (2015), due to the fact that we assumed C IV being co-spatial with the localised and relatively compact ($\sim 10 \text{ arcsec}^2$) regions where He II is emitted. We will present arguments regarding the validity of this assumption in Section 6.4. In the scenario of co-spatial C IV and He II emission our upper limits on C IV translate into upper limits of < 1 , < 1.4 , < 1 of C IV / He II in region “south”, “north”, and “LAB 8”, respectively.

6. Discussion

6.1. On interpreting the moment maps of Ly α from LAB 1 as a tracer of gas kinematics

Before interpreting flux-weighted moment maps from Ly α as a tracer of gaseous motions, we need to assess how Ly α radiative transfer effects may have influenced these measurements. So far existing Ly α velocity fields from extended Ly α nebulae showing coherent large-scale motions have been observed around known (e.g. Arrigoni Battaia et al. 2018; Martin et al. 2019) or suspected (Prescott et al. 2015a) quasars. Details on the density distribution of the gas within those systems are still not settled, nevertheless it has been asserted that the strong ionisation field from the quasar produces a large fraction of Ly α photons throughout the

nebula in-situ via recombinations (e.g. Martin et al. 2014; Martin et al. 2019; Cantalupo et al. 2014, 2019). Nevertheless, it is also fact that small residual neutral H I fractions ($\lesssim 10^{-4}$) within the ionised halo result in high optical depths in Ly α . But it is suspected that radiative transfer modulations of the Ly α profile for an extended intrinsic Ly α radiation field are less dramatic compared to the integrated spectrum of a compact Ly α emitting source. The rationale is that the profile measured at each position in the nebulae only reflects small local velocity offsets between point of emission and surface of last scattering (Prescott et al. 2015a). Combined with finite spectral resolution then only a broadening of the Ly α line is expected, but no significant redshift offsets. This expectation appears consistent with our results obtained on the He II emitting regions in LAB 1. Moreover, literature redshifts of the with the blob associated galaxies do not show significant redshift offsets with respect to Ly α (McLinden et al. 2013; Kubo et al. 2016; Umehata et al. 2017). From this absence of redshift offsets we conclude that the first-moment map traces at least the gas-kinematics close to the embedded sources. For those galaxy near zones we then conjecture that significant amounts of Ly α photons be produced in-situ.

For interpreting the whole first-moment map as a tracer of the underlying gas kinematics at zones far from known galaxies in the blob we can not, however, directly adopt above argument. The detection of a polarised Ly α at large distances to the known galaxies, both in imaging polarimetry (Hayes et al. 2011) and spectropolarimetry (Beck et al. 2016), shows that significant fractions of the observed Ly α photons must have scattered into the line of sight after being emitted from a central source.

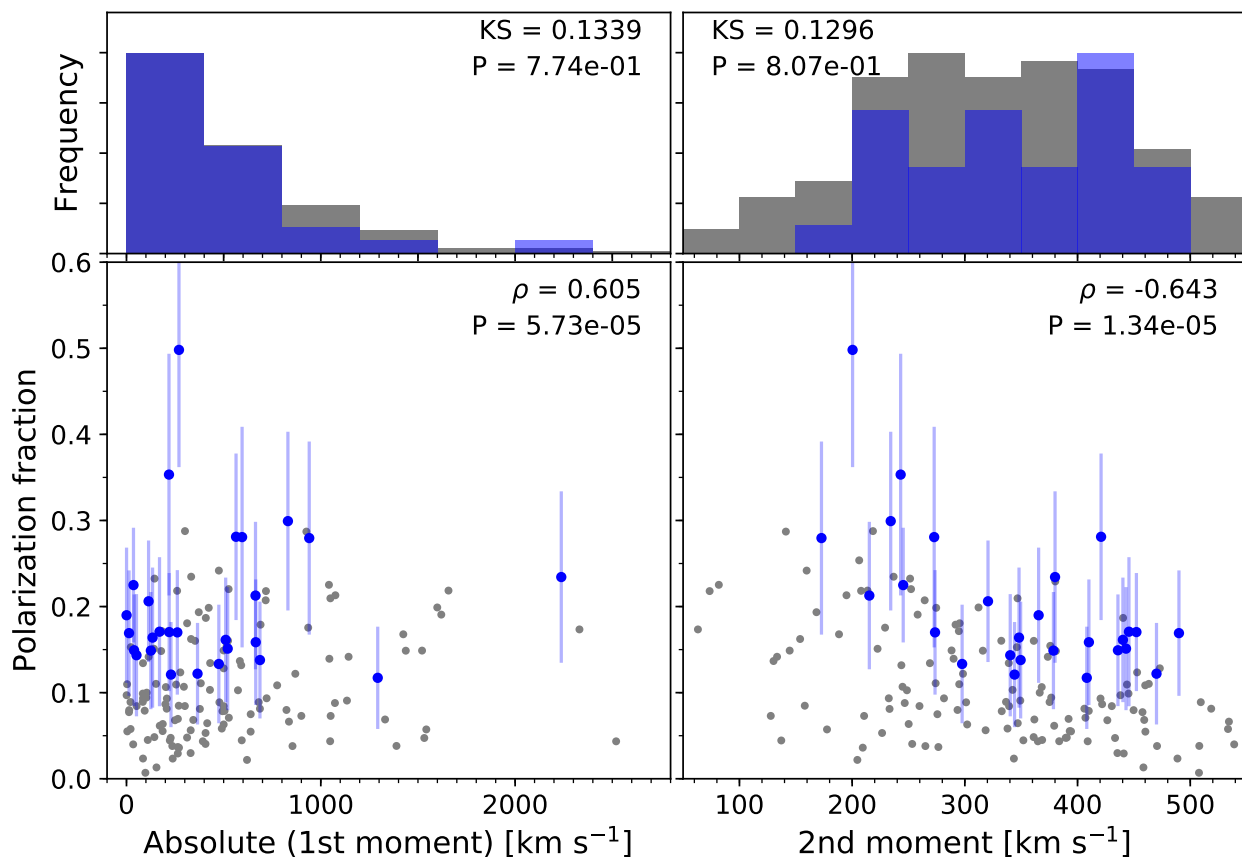


Fig. 12. A region-by-region comparison of the polarisation fraction (P) derived from VLT/FORS2 observations, with the kinematic properties of the $\text{Ly}\alpha$ emission derived in this paper. The *left panel* displays P for the absolute value of the first moment (the line-of-sight velocity), while the *right panel* shows P for the from the second moment derived velocity dispersion. Gray points show every spatial element for which polarimetric quantities have been calculated (see Figure 2 of Hayes et al. 2011) for which P could be measured at better than 5 per cent. Blue points show the regions in which P is detected at significance better than 2σ . Spearman's rank correlation coefficient (ρ), and its associated P -value are shown in each figure. The histograms above each plot shows the distribution of properties from the lower abscissae for both spaxels where P is significant at 2σ and where the polarisation is not detected. The values from the two-sample KS-statistic, and the associated P value presented in each panel show that the polarised spaxels are consistent with being drawn from the parent distribution, and that the trends do not result from a biased selection.

We will discuss these results in more detail in Sect. 6.2, where we present a hybrid analysis between the imaging polarimetry results and our MUSE data. According to theory (Dijkstra & Loeb 2008, e.g.) the observed polarisation signal in $\text{Ly}\alpha$ stems from scattered photons within the wing of the absorption profile. Hence, while these photons preserve information regarding the kinematics of the last-scattering surface, they will be red- or blue-shifted (depending on the kinematics of the scattering medium) with respect to the overall kinematics of the gas. Therefore, in a scenario where only scattered $\text{Ly}\alpha$ photons are observed at large distance to the embedded sources, the measured first-moments would be biased towards higher or lower velocities compared to the true gas kinematics. This could potentially increase the observed amplitude of an observed velocity gradient.

The above scenario requires that a significant amount of $\text{Ly}\alpha$ photons is released by the dust enshrouded systems. The possibility of this process is indicated by the detection of $\text{Ly}\alpha$ emission from nearby ultra-luminous infrared galaxies (Martin et al. 2015a). Feedback driven outflows powered by the star-formation from those systems is believed to create the required $\text{Ly}\alpha$ escape channels. Evidence for the required feedback effects at the positions of the galaxies comes from our higher-moment analysis discussed below (Sect. 6.3), but also from the spectropolarimetry

measurements by Beck et al. (2016). These authors find that the polarisation signal is increased in the wings of the $\text{Ly}\alpha$ profile, especially near the embedded galaxies. According to recent $\text{Ly}\alpha$ radiative transfer models of Eide et al. (2018) this is an expected polarisation signature in the presence of outflowing gas. Moreover, the $\text{Ly}\alpha$ escape channels produced by gaseous outflows can potentially also act as escape channels for ionising photons from the embedded systems, thus a significant fraction of those photons might indeed be available to power the emission from the blob via recombination. Empirical evidence for such a process have also been observed in the nearby universe (Herenz et al. 2017a; Bik et al. 2018; Menacho et al. 2019). Thus, in addition to $\text{Ly}\alpha$ scattering in far from the embedded galaxies, we also expect that a significant fraction of $\text{Ly}\alpha$ radiation is produced in-situ at larger distances from the known embedded sources. Both the detection of He II emission far from known galaxies as well as indications from the higher-moment maps (Sect. 6.3.3) argue for this scenario. Hence, the observed emission from the galaxy far-zones is rather a superposition of scattered and in-situ produced $\text{Ly}\alpha$ emission. This potentially mitigates the bias in the first moment maps that would result from pure $\text{Ly}\alpha$ scattering.

To summarise, we presented qualitative arguments in favour of interpreting large-scale coherent features in the first-moment map from $\text{Ly}\alpha$ as tracers of the gaseous motion in the system.

These qualitative arguments are, as of yet, not tested for Ly α radiative transfer simulations in realistic Ly α blob environments. As we will also discuss further below, radiative transfer effects are, however, expected to strongly influence the Ly α line-width and the derived moments of higher order. We suggest that the here presented non-parametric moment-based measurements of the line profiles present a starting point to summarise the complexity of the encountered profiles in LAB environments.

6.2. Combined analysis of Ly α line profile morphology and imaging polarimetry

Hayes et al. (2011) studied LAB1 using the FORS2 polarimeter at VLT in order to spatially map the polarimetric properties of the Ly α emission, including the Stokes vectors (Q and U), the polarised light fraction (P) and angle of the linear polarisation vector (χ). The resulting in maps of P and χ were qualitatively consistent with theoretical predictions by Lee & Ahn (1998), Rybicki & Loeb (1999), and Dijkstra & Loeb (2008), and implied a geometry in which Ly α is produced inside, or close to the central regions of the highest Ly α surface brightness (at the positions of the later discovered ALMA sources 1 and 2) and scattered at large impact parameters from the plane of the sky to the sight-line of the observer. However the imaging polarimetry data of Hayes et al. (2011) contained no information regarding the kinematic properties of the Ly α emission, and we could not study where in the Ly α line profile the polarisation signal is imparted onto the total Ly α surface brightness. To remedy this Beck et al. (2016) conducted spectroscopic polarisation observations with the same instrument, to study P and χ as a function of frequency. Those observations showed that the wavelength dependence of P is small near line centre, but rises towards the wings. This data contained frequency and kinematic information, but only at eight positions identified across the 1'' wide slit. Due to the low efficiency of the FORS2 polarimeter these studies were limited to the regions of highest surface brightness (Beck et al. 2016, their Figure 3).

In this Section we use the 3D spectroscopy provided by MUSE to shed some light on the origin of the polarisation signal. We perform a hybrid study, and contrast the spatially varying, but spectrally-integrated measurements of P and χ with the Ly α kinematics using 3D spectroscopy. Hayes et al. (2011) used Voronoi tessellation to locally enhanced the SNR in the individual beam-images, and we employ here the same binning patterns to the MUSE data. To this aim we aligned FORS2 Ly α intensity images with the MUSE data, and propagate this astrometric information into the maps of P , χ , and the binning pattern. For every Voronoi tessellated cell we then extract the corresponding spaxels from the MUSE datacube, and compute the moment based statistics described in Section 5.3.

Figure 12 shows the results, where we display the absolute value of velocity offset from $z_{\text{Ly}\alpha} = 3.1$ (left panel) and the velocity dispersion (right panel). We elect to show the absolute value of the first moment because polarisation signal imparted by blue- and red-wing scattering should manifest in the same P (Dijkstra & Loeb 2008), which is not discernible information from line-integrated intensity measurements in imaging polarimetry. We find a positive correlation between P and the absolute line-of-sight velocity, and also an anti-correlation between P and the velocity dispersion. That Ly α should exhibit higher degrees of polarisation for narrow lines is a curious result, and may stem from several effects.

In order to impart the highest polarisation fractions, scattering in the wing of the frequency redistribution profiles needs to

be enhanced (Dijkstra & Loeb 2008; Eide et al. 2018). Clearly this cannot be the case for a scattering medium that is static, and sees the Ly α radiation field close to line-centre, where core scatterings will occur. Some velocity offset is needed, which would imply that high P should avoid $|\Delta v_{\text{los}}| = 0$. This was the motivation for the outflowing shell models presented in Dijkstra & Loeb (2008). Moreover, in the presence of a large $|\Delta v_{\text{los}}|$, the velocity dispersion cannot be significantly larger than the absolute offset, as this will return a higher column density of gas back towards line-centre, which would maintain a high degree of core scattering. In a complicated, 3-dimensional environment with multiple sources of Ly α photons and certainly many velocity components of scattering gas, we speculate that the highly polarized regions will favor velocity shifts and narrow lines, which is precisely what Figure 12 shows.

If the Ly α photons are produced by the galaxies and scatter at large impact parameters, we would expect these photons to reflect the properties of the circumgalactic hydrogen gas, occupying a narrower range of velocities than the turbulent interstellar H II regions that are disrupted by stellar feedback. Such a distribution of velocities would also likely be seen if the Ly α is produced in-situ, but in this case it is harder to produce the polarisation pattern: this would still require photons to travel distances of $\gtrsim 10$ kpc (\sim one resolution element) before scattering. Secondly, regions with narrower line profiles may also be the result of gas along the line-of-sight occupying a narrower range of velocities, which may work against many resonant scattering events that would de-polarise the radiation. Nevertheless, we will argue in Sect. 6.3.3 that the line profiles in some regions of high-velocity shifts show signs for a combination of in-situ Ly α production and scattering.

6.3. Insights into LAB 1 from the spatially resolved line-profile analysis

6.3.1. Large-scale gas kinematics from the first-moment map

We concluded in Sect. 6.1 that the first-moment map from Ly α (Figure 7, left panel) can be used to trace the large scale kinematics of the gas within the blob. As apparent from that map, the blob shows a coherent large-scale velocity gradient from receding velocities on its eastern side to approaching velocities on its western side. This large scale velocity gradient encompasses LAB 1 and the northern neighbour LAB 8. Moreover, the newly detected shell-like region in the south-west (SW) of the blob is completely blue-shifted, thus seemingly follows the large scale E–W velocity gradient. Furthermore, also within the shell a gradient from NW to SE is seen. The velocity field is mostly coherent over ~ 150 kpc and shows significant perturbations only on smaller ($\lesssim 30$ kpc) scales.

We quantify the amplitude of the large-scale velocity shear as $v_{\text{shear}} = (v_{\text{max}} - v_{\text{min}})/2 = 1304 \text{ km s}^{-1}$, where v_{max} and v_{min} are the lower and upper 5th percentile of the observed first moments throughout the blob (this choice of percentiles is robust against outliers while sampling the true extremes of the distribution). Coherent large scale velocity fields of such large amplitude appear to be rare amongst extended Ly α nebulae around quasars at redshifts similar to LAB 1 (Borisova et al. 2016; Arrigoni Battaia et al. 2019). Nevertheless, a few comparable examples do exist: object 3 in Borisova et al. (2016), the QSO UM 287 studied in Martin et al. (2015b) and Martin et al. (2019), as well as object 13 from Arrigoni Battaia et al. (2019) that was described in detail in Arrigoni Battaia et al. (2018). Moreover, two of the four QSOs in the recent $z \sim 6$ sample by Drake et al. (2019) show

coherent kinematics, while the other two objects show highly irregular and disturbed velocity fields.

We may hypothesise that the preponderance of disturbed velocity fields around QSOs is due to AGN feedback effects. However, in the case of LAB 1 it became also evident that high-S/N observations were necessary to unveil its coherent large scale motions. Previous IFS observations of LAB 1 of significantly less depth (and of lower spatial resolution) were rather indicative of a more chaotic velocity field (Bower et al. 2004; Weijmans et al. 2010). Thus, the noisy appearance in the majority of the velocity fields from Borisova et al. (2016) and Arrigoni Battaia et al. (2019) might also be caused by the lower S/N in faint regions due to the snapshot nature of both surveys.

The most striking feature of the LAB 1 velocity field is that its orientation is perpendicular to its morphological principal axis (Figure 7, left panel). The existence of such a large-scale coherent velocity field of high-amplitude appears in qualitative agreement with theoretical predictions of hydro-dynamical simulations in a Λ CDM framework. In particular it is a natural outcome of the filamentary nature of the cosmic web and the predicted existence of dense cold-gas streams that can penetrate deeply into dark-matter potential wells without being shock-heated by the gravitational potential (see review by Stewart 2017). However, the perpendicular alignment between the velocity field and the principal axis means that the angular momentum vector of the gas in LAB 1 is aligned parallel with the principal axis. Simulations in the Λ CDM framework predict that the angular momentum vector and the elongation of the dark matter haloes – including their gaseous and stellar contents – show correlated properties with the surrounding large-scale structure of the cosmic-web (e.g. Forero-Romero et al. 2014; Libeskind et al. 2018; Codis et al. 2018; Wang & Kang 2018, and references therein). These studies predict that, on average, the angular-momentum of high-mass haloes ($\gtrsim 10^{12} M_{\odot}$) is expected to be orthogonal to their major axis, which is expected to be aligned parallel with the connecting filament of the cosmic web. Thus, the observed alignment between morphological principal axis, which we naively interpret as the direction of the major cosmic web filament (as suggested by Erb et al. 2011), renders LAB 1 as an outlier from the theoretically expected average for high-mass haloes.

We speculate that the deviation from the theoretically expected norm in LAB 1 is caused by the complexity of the surrounding large-scale structure. We regard the observed multi-filamentary morphology of the blob, with one filament extending to the SE in the direction of the two newly identified LAEs, and another filament connecting to the shell-like region in SW as evidence for such a complex environment. In fact, the SSA 22 proto-cluster, which hosts LAB 1 and LAB 8, is one of the most-massive structure known in the high-redshift universe (see Kikuta et al. 2019 for another extreme overdensity at $z = 2.84$). In such a high- z high-density peak of the universe a complex interwoven network of filaments is expected. Indeed, recent MUSE observations ($t_{\text{exp}} \approx 4$ h) by Umehata et al. (2019) have revealed such a cold-gas network in Ly α at the core of SSA 22, located $4.8'$ (2.19 Mpc) north-east of LAB 1. Interestingly, also this structure shows a mix of perpendicular and parallel aligned large-scale velocity gradients with respect to the filamentary structure (Umehata et al. 2019, their Fig. 3). Thus, in a dense environment where filamentary nodes arrive from various directions, alignment and misalignment between large-scale structure and angular momentum are observed. The complexity of angular momentum alignments in dense regions was studied in simulations by Lee et al. (2018), who also showed that in these

environments the orientation of angular momentum vector is expected to change frequently and significantly. In such a scenario the observed alignment of LAB 1's angular momentum can be reconciled as an early evolutionary stage of a massive galaxy.

6.3.2. Small-scale kinematical perturbations in the first-moment map

As mentioned before, the coherent velocity field of LAB 1 shows also various perturbations on smaller scales. One prominent perturbation occurs at the position of the Lyman break galaxy SSA22a-C11, where the velocity shears from north to south, i.e. almost perpendicular to the apparent large-scale motion. In this region the velocity field varies from $\sim 450 \text{ km s}^{-1}$ to $\sim -1500 \text{ km s}^{-1}$ just within $2''$ or 15 kpc in projection. It appears as if Ly α traces the velocity field of this individual bright galaxy that is not aligned with the blob's large scale velocity field. Such misalignments of sub-haloes are also in qualitative agreement with the theoretical studies mentioned in the previous section (e.g. Codis et al. 2018). However, this disturbance of the velocity field may also be caused by feedback effects. Less prominent disturbances are apparent near the sub-mm detected sources ALMA 1 and ALMA 2. Here, as we will discuss below in Sect. 6.3.3, the analysis of the higher order moment map will provide further arguments in favour star-formation driven winds and/or outflows.

While the small-scale perturbations may be caused by individual velocity fields of the embedded galaxies and/or star-formation driven winds or outflows, we also have to consider the alternative (but not competing) hypothesis that they may in fact represent evidence for cold-flow multi-filamentary inflows. Especially Martin et al. (2019) presented recently a quantitative framework to fit the expected kinematic signatures from cold-flow accretion streams to Ly α intensity weighted velocity maps. These authors motivate their parametric ansatz by numerical simulations of galaxy that exhibits cold filamentary inflows. The velocity field of this simulation was found to be optimally described by a large-scale rotating component that is modulated by radially and azimuthally varying components. These modulations are shown to capture the kinematic perturbations caused by the filamentary cooling flows. Martin et al. (2019) show that these parametric models also provide an excellent fit to the observed Ly α velocity fields of two large extended Ly α nebulae around radio-quiet quasars. We find that the qualitative appearance of velocity field modulations caused by the cooling flows in the Martin et al. ansatz bears similarity to the small scale perturbations seen in LAB 1's first-moment map. A quantitative treatment with the Martin et al. ansatz is, however, beyond the scope of the present analysis.

6.3.3. Interpretation of higher-order moment maps

Empirical insights into the Ly α photon production and/or scattering mechanisms within the blob can be gained from our maps of the Ly α line-width (Figure 7, right panel), its skewness, its kurtosis κ , as well as its bi-modality (Figure 8). In the following we will discuss several notable features in those maps. By visually inspecting the spaxels in each of the discussed regions we ensured that the mapped values are indeed representative of the observed line profile morphology.

The highest line-widths ($\sigma_v \gtrsim 500 \text{ km s}^{-1}$) are observed N and S of ALMA 1 and ALMA 2. Towards the north this high dispersion regions shows a V-shaped morphology that traces the

edges of the prominent “bubble” feature seen in the narrow-band image (Figure 5). While Ly α shows no pronounced double peaked profile ($b \gtrsim 2.6$) at the position of ALMA 1 and ALMA 2, more pronounced double peaks are observed in the V-shaped region ($b \sim 2$), with the NE arm showing the most pronounced double peaks ($b \lesssim 1.8$). Thus, while it is tempting to interpret the broad widths close to the sub-mm source as gas that is kinematically hotter due to feedback from the galaxies, the measured large width of the profiles in those regions is rather the result of double component Ly α profiles, i.e. Ly α radiative transfer.

However, we might witness possible signatures of outflowing gas traced by the Ly α skewness at the position of ALMA 1, where the Ly α profiles show a pronounced skew towards the blue ($s \lesssim -0.3$). Interestingly, the Ly α profiles in some of the Martin et al. (2015a) ULIRGs show blue-skewed profiles. Martin et al. (2015a) interpret these blue-wings as outflow signatures, with the Ly α in the wing being produced by gas cooling within the outflow. Also SE of ALMA 3 strong blue-skewed profiles indicative of an outflow are observed. This is corroborating the inference by Umehata et al. (2017) who argued that the properties of the [C II] 158 μ m emission from ALMA 3 are indicative of an interaction between a galactic outflow with an intergalactic gas stream.

As can be seen from Figure 7 the line-width of Ly α is narrower in the outskirts of the blob. Both the shell-like region in the SW, the filament emanating to the N and connecting to LAB 8, as well as the filament emanating to the NE are characterised by $\sigma_v \lesssim 200 \text{ km s}^{-1}$. However, as traced by the higher-moment based statistics (Figure 8), even in those regions the observed Ly α line profiles appear to be quite complex. For example along the LAB 1 - LAB 8 connecting filament the line profile is strongly skewed to the red ($s \gtrsim +0.5$). Most prominently this structure emerges as a red band in the skewness map. Throughout most of this filament the discriminatory power of the adopted bi-modality indicator is weak ($2.5 \gtrsim b \gtrsim 3$). However, visual inspection of the line profile hints at least in some places at the appearance of a secondary weaker red peak as cause for the measured red skew. For the NE filament observationally the situation is more clear, here the profile is clearly double peaked ($b \lesssim 2.5$, see also example spectrum in panel 1 of Figure 6), mostly with a weaker blue component. Both the red-skewed profiles with a potential secondary peak, as well as the double peaked profiles are likely caused by radiative transfer. As we discussed above (Sect. 6.2), the strongest polarisation signal arises in regions of smaller line-width ($\sigma_v \lesssim 250 \text{ km s}^{-1}$), also supportive of Ly α scattering from a central source. Hence, the low-line width regions in the outskirts and in the filamentary regions hint at dense patches of gas where Ly α scattering takes place. The filamentary morphology of some of these patches is morphological reminiscent of cooling-flows, but whether the dominant Ly α signal is produced by cooling or photo-ionisation in those regions remains unclear. At least the line profiles in those regions appear consistent with a super-position of in-situ produced Ly α photons (dominant peak) and scattered Ly α radiation (wing or second component).

Another peculiar feature in our higher moment-based maps is found at the N edge of the bubble. Here the profile is significantly skewed ($s \gtrsim +0.7$) and described by a single-component ($b \gtrsim 3$) profile with a pronounced wing ($\kappa \approx 4$). The bubble or cavity was already remarked as a peculiar feature in LAB 1 by Bower et al. (2004). As a possible scenario Bower et al. (2004) discuss, that the bubble is filled by hot ionised gas. Bower et al. (2004) speculate that a potential radio-jet from the sub-mm

sources could have heated this gas. In this scenario the skewed Ly α line arises in the region where the beamed emission is being slowed down by the denser cold-gas. Observational evidence for radio-emitting gas having and influence on the Ly α emission properties have been presented for radio loud quasars and radio galaxies (e.g. Humphrey et al. 2007; Roche et al. 2014; Borisova et al. 2016), but the physical details are not understood. Given the lack of detected radio emission from LAB 1, this scenario remains speculative. Thus, the alternative hypotheses from Bower et al. (2004) that the cavity has been blown by star-formation driven wind can not be excluded. The detection of He II emission in the vicinity of the bubble is, regardless of the driving mechanism, likely linked to shock heating effects within the shell. Evidence for this scenario will be presented in the following Sect. 6.4.

Lastly, we note that at the position of C11 the Ly α profile is single-peaked ($b > 3$), but shows significant tails towards both the blue and red ($\kappa > 3$). Inspecting the profile from C11 we find that these wings appear to have substructure in the form of two additional peaks (see also example spectrum 7 in Figure 6). This triple-peaked structure is reminiscent of the Ly α profile from a multiply lensed-galaxy by Rivera-Thorsen et al. (2017), although not as extreme. Rivera-Thorsen et al. (2017) showed, that triple peaked Ly α profiles are indicative of low-covering fractions of neutral gas along the sight-line (see also Behrens et al. 2014). Thus, such galaxies potentially leak ionising radiation along the sight-line. Indeed, recently Rivera-Thorsen et al. (2019) confirmed the ionising photon leakage from their system. Thus, although C11 is located in an extremely dense environment, at least in its vicinity most of the gas appears highly ionised, thereby possibly promoting the escape of ionising radiation.

6.4. He II emission from the LAB: Driven by feedback, cooling flows, or hard ionising radiation?

In Sect. 5.5 we reported on the detection of three distinct extended He II emitting zones with $\text{SB}_{\text{HeII}} \sim 10^{-19} \text{ erg s}^{-1} \text{ cm}^{-2} \text{ arcsec}^{-2}$. Extended He II emission is commonly observed within the extended Ly α emitting regions surrounding high- z radio galaxies (e.g. Villar-Martín et al. 2007; Morais et al. 2017; Marques-Chaves et al. 2019). Broad line profiles and alignments with the radio-jet axes indicate that He II is powered by jet-gas interactions in those objects. Detections of He II emitting zones within the extended Ly α nebulae surrounding radio quiet quasars or in LABs not directly associated with an AGN appear more difficult to interpret (Scarlata et al. 2009b; Prescott et al. 2009; Cai et al. 2017; Cantalupo et al. 2019; Humphrey et al. 2019). Different explanations have been put forward, e.g. with Scarlata et al. (2009b) favouring cooling-radiation in their system, Prescott et al. (2009) arguing for photo-ionisation by an AGN or an extremely metal poor stellar population in their object, while Cai et al. (2017) reason that their extended He II zone is powered by shocks. We now try to constrain the physical mechanisms responsible for the extended He II emission in the blob. To this aim we will also consider the derived upper limits on C IV emission from the He II emitting zones (Sect. 5.6).

Our upper limit for C IV emission within the He II emitting zones ($8 \times 10^{-19} \text{ erg s}^{-1} \text{ cm}^{-2} \text{ arcsec}^{-2}$, Sect. 5.6) appears, at first sight, less constraining than the previous upper limit of $7.4 \times 10^{-19} \text{ erg s}^{-1} \text{ cm}^{-2} \text{ arcsec}^{-2}$ from narrow-band observations by Arrigoni Battaia et al. (2015). However, the comparison has to be treated with caution, as their upper limit estimation as-

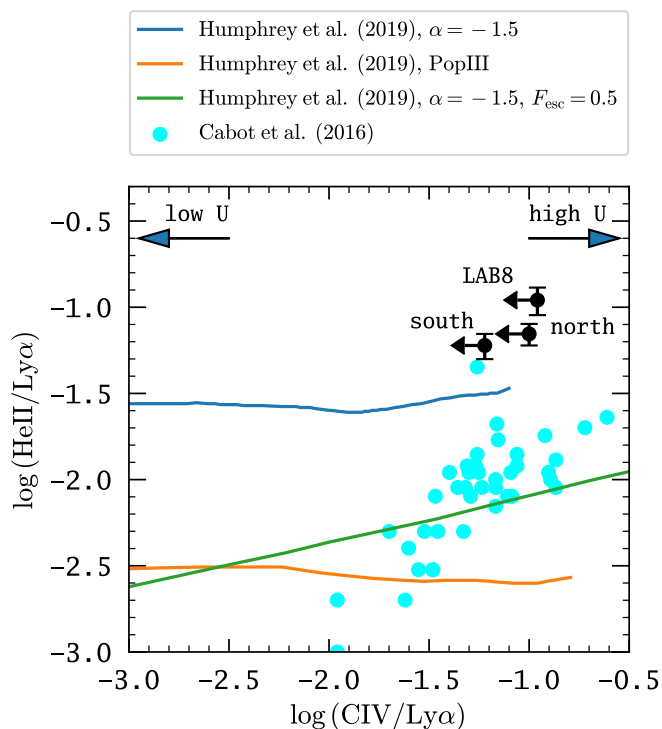


Fig. 13. Measured He II/Ly α ratios vs. upper limits on C IV/Ly α ratios for the three regions where we detect He II emission in the LAB. We also show tracks of recent photoionisation models by Humphrey et al. (2019) for low metallicity ($Z = 0.01Z_{\odot}$) low-density gas in the circumgalactic medium of AGN host-galaxies (blue and green curve, see text for details) or Pop-III star-forming galaxies (orange curve). The tracks show predicted line ratio for a range of different ionisation parameters U (defined as $U \propto Q/r^2 n_{\text{H}}$, where Q is the rate of hydrogen ionising photons, r is the distance from the ionising source, and n_{H} is the hydrogen density of the illuminated medium), varying from $U = 0.25$ for the highest C IV/Ly α ratios to $U \approx -2.5$ where C IV/Ly $\alpha = -3$. We also show the predicted line-ratios from ab-initio hydrodynamical simulations of 49 $z = 3$ LABs by Cabot et al. (2016).

summed constant C IV emission over the whole area of the blob ($\sim 200 \text{ arcsec}^2$). But, given the different ionisation potentials of the emitting species and different excitation mechanisms, this assumption can not be made. We here assumed that C IV emission is confined to the three He II emitting regions ($\lesssim 10 \text{ arcsec}^2$). The assumption of overlapping C IV and He II emission appears a good first-order approximation in scenario where C IV and He II act as a coolant of shock heated gas, as for both lines the maximum emissivity is obtained in a similar gas phase of $T \sim 10^5 \text{ K}$ (Cabot et al. 2016), where C IV is driven through collisional excitations of C^{3+} (ionisation potential 47.9 eV) while He II is originating from the recombination cascade of collisionally ionised He^{2+} (ionisation potential 54.4 eV). Nevertheless, the C IV emissivity also peaks in a region of slightly lower density ($n_{\text{H}} \sim 2 - 5 \text{ cm}^{-3}$) compared to He II ($n_{\text{H}} \sim 5 - 20 \text{ cm}^{-3}$), thus C IV could potentially also be more extended (Cabot et al. 2016). This effect could be further enhanced by the resonant nature of C IV (see also Berg et al. 2019). On the other hand, if photo-ionisation from a AGN produces C^{4+} (ionisation potential 64.4 eV) that emits C IV as a result of recombinations, the C^{4+} zone would be confined within the He^{2+} zone.

Two of our three detected zones of He II emission are in close vicinity to confirmed star-forming galaxies within the blob. It appears natural to suspect that there either hard ionising radia-

tion from the galaxies or shock heated gas due to feedback effects is responsible for driving the He II emission. The nearly co-spatial occurrence with the galaxies is qualitatively consistent with the models from Cabot et al. (2016). These authors predict that shock-heated gas from supernovae driven winds should be the main source of He II emission, with $\sim 70\%$ of He II photons stemming from this process. Their model treats both Ly α radiative transfer and dust-extinction effects, as well as photo-ionisation from a canonical stellar population. In Figure 13 we compare our measured He II/Ly α ratios with the results from the hydrodynamical simulations by Cabot et al. (2016). As can be seen our measured He II/Ly α ratios are above the ratios predicted by the models, while our upper limits on C IV/Ly α are compatible with their models.

In Figure 13 we also compare our derived line ratios and upper limits to tracks from the recent photo-ionisation models by Humphrey et al. (2019). These tracks were computed for different ionising sources illuminating low-metallicity ($Z = 0.01Z_{\odot}$) gas. We show the resulting predictions for photo-ionisation by an idealised quasar (described by a $F_{\nu} \propto \nu^{\alpha}$ power-law continuum spectral energy distribution with $\alpha = -1.5$, blue curve), an idealised quasar whose ionising continuum has been modified by intervening cold-gas that absorbs 50% of the ionising photons (green curve) and a fiducial zero-metallicity stellar population (modelled by a $8 \times 10^4 \text{ K}$ black body). These models encode the hydrogen density $n_{\text{H}} [\text{cm}^{-3}]$, the rate of hydrogen ionising photons $\dot{Q} [\text{s}^{-1}]$, and distance to the ionising source $r [\text{cm}]$ within the dimensionless ionisation parameter $U = \dot{Q}/(4\pi c n_{\text{H}} r^2)$. The He II emitting region “south” He II is observed at distances of $\sim 10 - 30 \text{ kpc}$ from ALMA 1 and ALMA 2. Asserting $\dot{Q} \leq 10^{55} \text{ s}^{-1}$, which is the maximum value to power the blob via photo-ionisation, typical values for U are in the range $\log U \leq -0.5 - -2.5$ for densities of 0.1 cm^{-3} to 10 cm^{-3} at a distance of $r = 10 \text{ kpc}$ ($\log U \leq -1.8 - -3.8$ for $r = 30 \text{ kpc}$). For region “north”, which is at greater distances to ALMA 1 and ALMA 2, and region “LAB 8”, which is in the vicinity of a more moderate star-forming galaxy, even lower values of U appear reasonable. As can be seen from Figure 13, the Humphrey et al. (2019) photo-ionisation models predict significantly lower He II/Ly α ratios than observed within the He II emitting zones of LAB 1.

We show in Figure 13 predictions of the models only for $-2.5 < \log U < 0.25$, noting that both the He II/Ly α and C IV/Ly α ratios decrease significantly for $\log U < -2.5$. Within the displayed range the He II/Ly α ratio exhibits a weak dependence on U , while the C IV/Ly α ratio rapidly decreases with decreasing U . The reason for the almost constant He II/Ly α ratio is that in the simulated low-metallicity gas the fraction of He^{++} ions remains saturated for a $U \gtrsim -2.5$ photo-ionisation field. However, for $U < -2.5$ He II/Ly α will start to decrease significantly. The large decrease in C IV/Ly α for decreasing U is driven by both the reduction in electron temperature (resulting in lower collision rates for C^{3+}) and the decreasing fraction of C^{3+} ions for smaller values of U . However, it is also apparent that the photo-ionisation tracks overlap with the predictions from the ab-initio simulations by Cabot et al. (2016) in which shock-heated emission dominates.

A similar degeneracy was commented upon by Arrigoni Battaia et al. (2015), who computed a different set of AGN photo-ionisation models predicting the He II/Ly α vs. C IV/Ly α diagnostic as a function of U . These authors modelled the expected line ratios in solar-metallicity optically-thick and optically-thin gas. Their optically-thin models are compatible with our He II/Ly α ratios at very low ionisation parameters ($\log U \lesssim -2.5$), where C IV/Ly $\alpha \lesssim 10^{-2}$ (Figure 12 in Arrigoni Battaia et al. 2015),

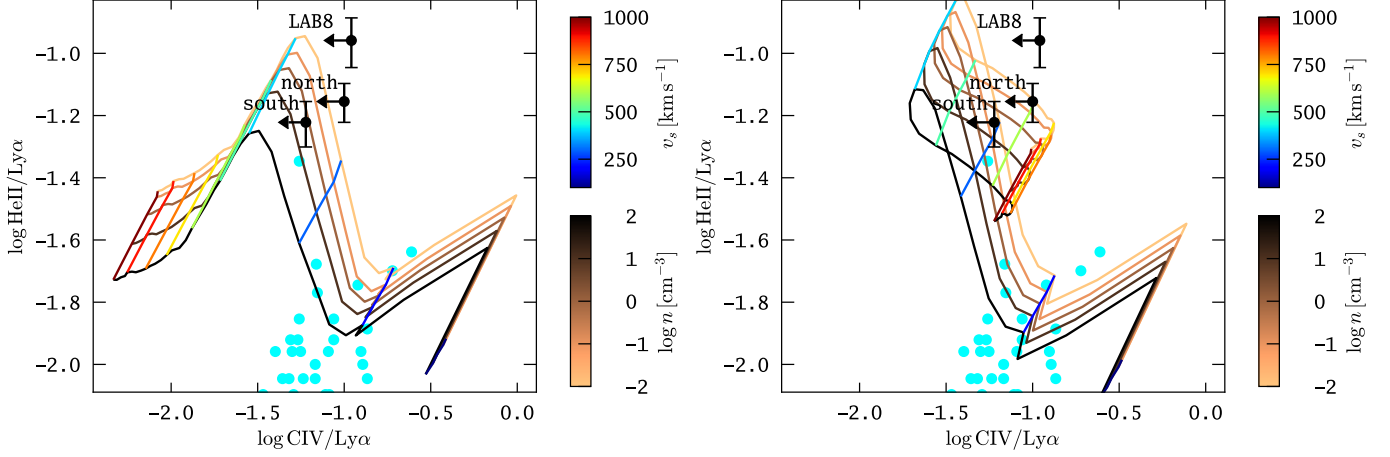


Fig. 14. Measured He II/Ly α ratios vs. upper limits on C IV/Ly α ratios for the three regions where we detect He II emission in the LAB compared to shock (*left panel*) and shock+precursor (*right panel*) models from Allen et al. (2008). We show all models for a constant magnetic parameter $B/n^{1/2} = 3.23 \mu\text{G}/\text{cm}^{3/2}$. The grids are color coded according to the density n_{H} of the pre-shocked region and the shock velocity v_s . We also show the predicted line-ratios from ab-initio hydrodynamical simulations of 49 $z = 3$ LABs by Cabot et al. (2016).

i.e. ≈ 10 times below our upper limit for this ratio. As discussed above, such low values of U are not unrealistic for the He II emitting zones within the LAB. On the other hand, their optically thick models (N_{H}) would require relatively high ionisation parameters to reproduce our observed He II/Ly α ratios. For those models then, the predicted C IV/Ly α values would be slightly below our upper limits. But, this region of the He II/Ly α vs. C IV/Ly α parameter space is also covered by shock models. This is illustrated by Figure 14, where we compare our measurements and upper limits to the predictions from shock models at solar metallicity by Allen et al. (2008). For those models we use the same parameters motivated by Arrigoni Battaia et al. (2015), and we refer to Sect. 5.2 of their publication for an in-depth discussion of the motivation and description of the models.

As evident by Figure 14, both shock and shock+precursor models can reproduce the observed He II/Ly α ratios for C IV/Ly α ratios that would be consistent with our upper limits for shock velocities of $v_s \sim 250 - 500 \text{ km s}^{-1}$. While for region “south” the observed line-width in He II appears compatible with those velocities, the other two regions show significantly narrower He II emission. However, especially the emission stemming from the pre-cursor arises in kinematically more quiescent gas which is photoionised by the hard-UV radiation from the shock. The measured line-widths might thus indicate that we observe He II emission from the pre-shock phase.

An alternative interpretation is provided in the models from Yang et al. (2006). These models suggest that extended zones of narrow ($\lesssim 250 \text{ km s}^{-1}$) He II emission within Ly α blobs are a signature of gravitational cooling radiation. We here observe He II in close vicinity to star-forming galaxies (regions “south” and “LAB 8”) and next to the expanding bubble within the blob (region “north”). Yang et al. (2006) predict the highest He II and Ly α surface brightness in close vicinity of the star-forming galaxies within the blobs. Considering only Ly α emission, a similar conclusion was recently reached by Trebitsch et al. (2016). In such a scenario then regions “south” and “LAB 8” might not be unambiguously identified with shock-heated gas. However, this scenario appears incompatible with He II emission from region “north”, as it is in close vicinity to strongly star-forming galaxies. Region “north” rather coincides with the edge of a ex-

panding shell where shocks are expected to occur. Hence, while our He II/Ly α measurements and our C IV/Ly α upper limits appear to favour shock-heated gas, we can not rule out contributions from cooling radiation in two of our three detected He II patches.

A potential caveat when comparing our measured line ratios with photoionisation models is that measurements were obtained within apertures that cover an projected area of $\sim 10^3 \text{ kpc}^2$. We expect realistically that gas within those regions exhibits a range of different densities and temperatures. However, the observed He II/Ly α ratios from photo-ionised gas from an embedded quasar will depend sensitively on the density distribution of the line emitting gas (Cantalupo et al. 2019). In fact, for any realistic density distribution the aperture integrated He II/Ly α ratio will always be lower than the intrinsic ratios within the volume covered by the aperture. Thus the quantitative comparison between our measured line ratios and upper limits to the models of Humphrey et al. (2019) must be treated with caution, as these models always assumed constant densities. Nevertheless, given the lack of direct evidence for AGN activity and the presented arguments in favour of other processes, AGN photoionisation appears to be the least likely cause for the extended He II emission.

7. Summary and conclusions

We presented MUSE observations of up to 17.2 h open shutter time of the prototypical SSA22a LAB 1 at $z = 3.1$. Our analysis revealed many previously unknown features of this enigmatic high- z object and provided detailed look into the early formation stage of a massive galaxy within an extremely dense environment. The main results of our study are the following:

1. Our IFS data reaches a limiting depth of $\approx 10^{-19} \text{ erg s}^{-1} \text{ cm}^{-2} \text{ arcsec}^{-2}$ in Ly α . This is significantly deeper than previous IFS observations of LAB 1 by Weijmans et al. (2010) that revealed Ly α down to $5.6 \times 10^{-18} \text{ erg s}^{-1} \text{ cm}^{-2} \text{ arcsec}^{-2}$. At this unprecedented depth we uncover several hitherto unknown features of the blob. Most prominently we find a filamentary bridge connecting LAB 1 with its northern neighbour LAB 8 and a shell-like arc towards the SW of LAB 1. Potentially another

filament is emanating to the SE in the direction of two newly identified faint LAEs. These filamentary features are visible both in the sequence of 2.5 Å narrow-band slices (Figure 3) as well as in the adaptive Ly α image (Figure 5). The newly uncovered structures are morphologically reminiscent of cold streams that are predicted to funnel cool gas into the potential wells of massive halos. As cooling flows are expected to align with the underlying filamentary large scale structure, the presence of multiple filaments pointing into various directions may imply that LAB 1 harbours a node in the cosmic web where a complex interwoven network of filaments arrives from various directions.

2. We find a ring-like structure slightly west of the photometric centre that is deprived in Ly α emission. While previous observations hinted already at the existence of this feature (Bower et al. 2004; Weijmans et al. 2010), the improved spatial resolution and sensitivity of our observations allow to slice through this shell in velocity space (Figure 3). The detection of He II emission at a He II/Ly α ratio consistent with expectations for shock heated gas in regions directly demarcating the “bubble” appears supportive of the hypothesis that we are observing a genuine cavity filled by hot ionised gas. Characteristic features in the Ly α line profile indicate that pressure exerted by the hot ionised gas drives an the expansion of the bubble (Sect. 6.3.3). Potential driving mechanisms for this expansion are a star-formation driven wind or radio emission from an obscured or faded AGN associated to the sub-mm source LAB1-ALMA2.
3. The Ly α profiles observed from the blob exhibit varying degrees of complexity (Figure 6). We tried to map the varying complexity of the blob by utilising a moment-based non-parametric analysis of the profiles (Sect. 5.3). This analysis provided us with maps of the line of sight velocity (central moment), the width of the line, its skewness, kurtosis, and bi-modality (Figure 7 and Figure 8). Especially within the central regions of the blob we find broad double- or even triple peaked profiles. Other regions are characterised by single peaked profiles that are sometimes skewed towards the blue or the red. The spatially varying complexity of the profiles likely encodes a mix of different Ly α photon production mechanisms: in-situ production from ionising sources and gravitational cooling, or both simultaneously. Moreover, projection effects from the line-of-sight passing through multiple filaments may also be responsible for the appearance of multiple peakse. Quantitatively disentangling the production mechanisms and projection effects based on the line profiles appears notoriously difficult, not at least due to a lack of comparable radioactive transfer simulations for Ly α blobs. We argue that the first-moment map is, despite the complexity of the profiles, a good tracer of the overall kinematics of the blob (Sect. 6.1). Several of the notable features in the higher-moment based maps appear to be well explained by feedback effects when they occur near the embedded galaxies. Characteristic features apearing distant to known galaxies likely stem from a by a mix of in-situ production and Ly α scattering (Sect. 6.3.3).
4. We find the highest degrees of Ly α polarisation in regions that exhibit high velocity shifts and narrow line profiles (Sect. 6.2 and Figure 12). These regions are far from known embedded galaxies. It appears that this result is consistent with theoretical expectations for Ly α scattering from a central source, although numerical simulations for Ly α polarisation in complex 3D environments have yet to be performed. Moreover, we argue that the observed Ly α emission from

those galaxy far zones is a combination of in-situ produced Ly α and scattered Ly α .

5. The line-of-sight velocity field of the blob is characterised by a large-scale velocity gradient that is oriented perpendicular to the morphological major axis of the blob (Figure 7, left panel). The observed shearing amplitude is $v_{\text{shear}} \approx 1300 \text{ km s}^{-1}$. The orientation of the velocity gradient implies a parallel alignment between angular momentum vector and major axis. This parallel alignment between major axis and angular momentum appears at odds with the theoretically expected average for massive halos (Sect. 6.3.1). We argue that this peculiar alignment reflects the complexity of the dense environment in which the blob resides. This leads us to speculate that LAB 1 is formed at the node of multiple intersecting filaments of the cosmic web.
6. We detect extended He II $\lambda 1640$ emission at three disjunct regions in the blob (Sect. 5.5 and Figure 10). Two of those regions surround known embedded galaxies, and the third region demarcates the expanding bubble. Our observations provide only upper C IV $\lambda 1549$ emission from those regions (Sect. 5.6). A comparison between predicted He II/Ly α and C IV ratios with shock- and photo-ionisation models from the literature with our measurements and upper limits appears to rule out photo ionisation from a hard ionising source as dominant production mechanism for He II (Sect. 6.4). Both gravitational cooling and feedback driven shocks appear as plausible mechanisms to drive the two He II emitting regions in vicinity of the embedded galaxies. However, the He II zone at the edge of the expanding bubble is likely powered by fast radiative shocks.

Our analysis shows that a lot of the mysteries that surround LABs can be solved with a substantial observational effort. The presented here deep MUSE observations of LAB 1 in combination with previous results at sub-mm wavelengths and polarisation measurements provide a clear picture regarding the Ly α emission mechanisms. Within the central regions of the blob ionising radiation and feedback effects appear to play a dominant role, but in the outskirts a potentially significant contribution of scattered Ly α radiation can be observed. Quantitatively disentangling these processes still proves challenging and numerical simulations of Ly α radiative transfer are needed for this purpose.

Being now equipped with a better understanding of the physical processes at play in LAB 1 we may ultimately ask questions regarding the evolutionary stage and fate of such a structure. Given the numerous strongly star-forming galaxies within the blob and the surrounding dense proto-cluster environment it appears natural to suspect LAB 1 as the progenitor of a massive cluster elliptical. The detection of He II emission likely signifies the importance of feedback effects in the early evolutionary stage of such systems. Moreover, our study highlights the potential importance of environmental effects on the kinematic properties of massive halos. As our study focused on a single object we can not establish any empirical trends in this respect, thus future studies of LAB samples at sufficient depth in proto-cluster environments are desirable.

Acknowledgements. E.C.H. thanks the extragalactic group at Stockholm University for a wonderful time and many insightful discussions during this project. E.C.H. also thanks Aaron Smith and Peter Laursen for useful comments during early stages of this project. This research made extensive use of the *astropy* package (Astropy Collaboration et al. 2018). All figures in this paper were created using *matplotlib* (Hunter 2007).

References

- Alexander, D. M., Simpson, J. M., Harrison, C. M., et al. 2016, *MNRAS*, 461, 2944
- Allen, M. G., Groves, B. A., Dopita, M. A., Sutherland, R. S., & Kewley, L. J. 2008, *ApJS*, 178, 20
- Ao, Y., Matsuda, Y., Beelen, A., et al. 2015, *A&A*, 581, A132
- Ao, Y., Matsuda, Y., Henkel, C., et al. 2017, *ApJ*, 850, 178
- Arrigoni Battaia, F., Hennawi, J. F., Prochaska, J. X., et al. 2019, *MNRAS*, 482, 3162
- Arrigoni Battaia, F., Prochaska, J. X., Hennawi, J. F., et al. 2018, *MNRAS*, 473, 3907
- Arrigoni Battaia, F., Yang, Y., Hennawi, J. F., et al. 2015, *ApJ*, 804, 26
- Astropy Collaboration, Price-Whelan, A. M., Sipőcz, B. M., et al. 2018, *AJ*, 156, 123
- Bacon, R., Accardo, M., Adjali, L., et al. 2010, in *Society of Photo-Optical Instrumentation Engineers (SPIE) Conference Series*, Vol. 7735, *Society of Photo-Optical Instrumentation Engineers (SPIE) Conference Series*
- Bacon, R., Conseil, S., Mary, D., et al. 2017, *A&A*, 608, A1
- Bacon, R. & Monnet, G. J. 2017, *Optical 3D-Spectroscopy for Astronomy* (Wiley-VCH Verlag GmbH & Co. KGaA)
- Bacon, R., Piqueras, L., Conseil, S., Richard, J., & Shepherd, M. 2016, *MPDAF: MUSE Python Data Analysis Framework*, *Astrophysics Source Code Library*
- Bacon, R., Vernet, J., Borisova, E., et al. 2014, *The Messenger*, 157, 13
- Barger, A. J., Cowie, L. L., & Wold, I. G. B. 2012, *ApJ*, 749, 106
- Beck, M., Scarlata, C., Hayes, M., Dijkstra, M., & Jones, T. J. 2016, *ApJ*, 818, 138
- Behrens, C., Dijkstra, M., & Niemeyer, J. C. 2014, *A&A*, 563, A77
- Berg, D. A., Chisholm, J., Erb, D. K., et al. 2019, *ApJ*, 878, L3
- Bik, A., Östlin, G., Menacho, V., et al. 2018, *A&A*, 619, A131
- Borisova, E., Cantalupo, S., Lilly, S. J., et al. 2016, *ApJ*, 831, 39
- Bower, R. G., Morris, S. L., Bacon, R., et al. 2004, *MNRAS*, 351, 63
- Bridge, J. S., Hayes, M., Melinder, J., et al. 2018, *ApJ*, 852, 9
- Brooks, A. M., Governato, F., Quinn, T., Brook, C. B., & Wadsley, J. 2009, *ApJ*, 694, 396
- Bădescu, T., Yang, Y., Bertoldi, F., et al. 2017, *ApJ*, 845, 172
- Cabot, S. H. C., Cen, R., & Zheng, Z. 2016, *MNRAS*, 462, 1076
- Cai, Z., Fan, X., Yang, Y., et al. 2017, *ApJ*, 837, 71
- Cantalupo, S. 2017, in *Astrophysics and Space Science Library*, Vol. 430, *Gas Accretion onto Galaxies*, ed. A. Fox & R. Davé, 195
- Cantalupo, S., Arrigoni-Battaia, F., Prochaska, J. X., Hennawi, J. F., & Madau, P. 2014, *Nature*, 506, 63
- Cantalupo, S., Pezzulli, G., Lilly, S. J., et al. 2019, *MNRAS*, 483, 5188
- Cappellari, M. & Copin, Y. 2003, *MNRAS*, 342, 345
- Chapman, S. C., Lewis, G. F., Scott, D., et al. 2001, *ApJ*, 548, L17
- Chapman, S. C., Scott, D., Windhorst, R. A., et al. 2004, *ApJ*, 606, 85
- Chapman, S. C., Windhorst, R., Odewahn, S., Yan, H., & Conselice, C. 2003, *ApJ*, 599, 92
- Childs, H. J. T. & Stanway, E. R. 2018, *MNRAS*, 480, 1938
- Chonis, T. S., Blanc, G. A., Hill, G. J., et al. 2013, *ApJ*, 775, 99
- Codis, S., Jindal, A., Chisari, N. E., et al. 2018, *MNRAS*, 481, 4753
- Conseil, S., Bacon, R., Piqueras, L., & Shepherd, M. 2016 [1612.05308]
- Davies, R., Agudo Berbel, A., Wozorrek, E., Ott, T., & Förster-Schreiber, N. M. 2010, in *Proc. SPIE*, Vol. 7735, *Ground-based and Airborne Instrumentation for Astronomy III*, 77356V
- Dekel, A. & Birnboim, Y. 2006, *MNRAS*, 368, 2
- Dijkstra, M. 2019, *Saas-Fee Advanced Course*, 46, 1
- Dijkstra, M. & Loeb, A. 2008, *MNRAS*, 386, 492
- Dijkstra, M. & Loeb, A. 2009, *MNRAS*, 400, 1109
- Drake, A. B., Farina, E. P., Neeleman, M., et al. 2019, *ApJ*, 881, 131
- Drake, A. B., Garel, T., Wisotzki, L., et al. 2017a, *A&A*, 608, A6
- Drake, A. B., Guiderdoni, B., Blaizot, J., et al. 2017b, *MNRAS*, 471, 267
- Eide, M. B., Gronke, M., Dijkstra, M., & Hayes, M. 2018, *ApJ*, 856, 156
- Erb, D. K., Bogosavljević, M., & Steidel, C. C. 2011, *ApJ*, 740, L31
- Forero-Romero, J. E., Contreras, S., & Padilla, N. 2014, *MNRAS*, 443, 1090
- Francis, P. J., Woodgate, B. E., Warren, S. J., et al. 1996, *ApJ*, 457, 490
- Geach, J. E., Bower, R. G., Alexander, D. M., et al. 2014, *ApJ*, 793, 22
- Geach, J. E., Narayanan, D., Matsuda, Y., et al. 2016, *ApJ*, 832, 37
- Gronke, M. & Bird, S. 2017, *ApJ*, 835, 207
- Haiman, Z., Spaans, M., & Quataert, E. 2000, *ApJ*, 537, L5
- Hayashino, T., Matsuda, Y., Tamura, H., et al. 2004, *AJ*, 128, 2073
- Hayes, M., Scarlata, C., & Siana, B. 2011, *Nature*, 476, 304
- Herenz, E. C., Hayes, M., Papaderos, P., et al. 2017a, *A&A*, 606, L11
- Herenz, E. C., Urrutia, T., Wisotzki, L., et al. 2017b, *A&A*, 606, A12
- Herenz, E. C. & Wisotzki, L. 2017, *A&A*, 602, A111
- Herenz, E. C., Wisotzki, L., Saust, R., et al. 2019, *A&A*, 621, A107
- Herenz, E. C. & Wisotzki, L. 2016, *LSDCat: Line Source Detection and Cataloguing Tool*, *Astrophysics Source Code Library*
- Hu, M. K. 1962, *IRE Transactions on Information Theory*, 8, 179
- Humphrey, A., Villar-Martín, M., Binette, L., & Raj, R. 2019, *A&A*, 621, A10
- Humphrey, A., Villar-Martín, M., Fosbury, R., et al. 2007, *MNRAS*, 375, 705
- Hunter, J. D. 2007, *Computing In Science & Engineering*, 9, 90
- Husemann, B., Worsack, G., Arrigoni Battaia, F., & Shanks, T. 2018, *A&A*, 610, L7
- Joye, W. A. & Mandel, E. 2003, in *Astronomical Society of the Pacific Conference Series*, Vol. 295, *Astronomical Data Analysis Software and Systems XII*, ed. H. E. Payne, R. I. Jedrzejewski, & R. N. Hook, 489–492
- Kennicutt, Jr., R. C. 1998, *ARA&A*, 36, 189
- Kereš, D., Katz, N., Weinberg, D. H., & Davé, R. 2005, *MNRAS*, 363, 2
- Kikuta, S., Matsuda, Y., Cen, R., et al. 2019, *PASJ*, 71, L2
- Kubo, M., Yamada, T., Ichikawa, T., et al. 2015, *ApJ*, 799, 38
- Kubo, M., Yamada, T., Ichikawa, T., et al. 2016, *MNRAS*, 455, 3333
- Laursen, P., Razoumov, A. O., & Sommer-Larsen, J. 2009, *ApJ*, 696, 853
- Laursen, P., Sommer-Larsen, J., & Razoumov, A. O. 2011, *ApJ*, 728, 52
- Lee, H.-W. & Ahn, S.-H. 1998, *ApJ*, 504, L61
- Lee, J., Kim, S., Jeong, H., et al. 2018, *ApJ*, 864, 69
- Lehmer, B. D., Alexander, D. M., Chapman, S. C., et al. 2009a, *MNRAS*, 400, 299
- Lehmer, B. D., Alexander, D. M., Geach, J. E., et al. 2009b, *ApJ*, 691, 687
- Libeskind, N. I., van de Weygaert, R., Cautun, M., et al. 2018, *MNRAS*, 473, 1195
- Loomis, R. A., Öberg, K. I., Andrews, S. M., et al. 2018, *AJ*, 155, 182
- Mallery, R. P., Mobasher, B., Capak, P., et al. 2012, *ApJ*, 760, 128
- Marques-Chaves, R., Pérez-Fournon, I., Villar-Martín, M., et al. 2019, *A&A*, 629, A23
- Martin, C. L., Dijkstra, M., Henry, A., et al. 2015a, *ApJ*, 803, 6
- Martin, D. C., Chang, D., Matuszewski, M., et al. 2014, *ApJ*, 786, 106
- Martin, D. C., Matuszewski, M., Morrissey, P., et al. 2015b, *Nature*, 524, 192
- Martin, D. C., O’Sullivan, D., Matuszewski, M., et al. 2019, *Nature Astronomy*
- Matsuda, Y., Iono, D., Ohta, K., et al. 2007, *ApJ*, 667, 667
- Matsuda, Y., Yamada, T., Hayashino, T., et al. 2004, *AJ*, 128, 569
- Matsuda, Y., Yamada, T., Hayashino, T., et al. 2011, *MNRAS*, 410, L13
- Mawatari, K., Yamada, T., Nakamura, Y., Hayashino, T., & Matsuda, Y. 2012, *ApJ*, 759, 133
- McLinden, E. M., Malhotra, S., Rhoads, J. E., et al. 2013, *ApJ*, 767, 48
- Menacho, V., Östlin, G., Bik, A., et al. 2019, *MNRAS*, 487, 3183
- Morais, S. G., Humphrey, A., Villar-Martín, M., et al. 2017, *MNRAS*, 465, 2698
- Mori, M., Umemura, M., & Ferrara, A. 2004, *ApJ*, 613, L97
- Morrison, J. E., Röser, S., McLean, B., Bucciarelli, B., & Lasker, B. 2001, *AJ*, 121, 1752
- Morrissey, P., Matuszewski, M., Martin, D. C., et al. 2018, *ApJ*, 864, 93
- Nilsson, K. K., Fynbo, J. P. U., Møller, P., Sommer-Larsen, J., & Ledoux, C. 2006, *A&A*, 452, L23
- Ott, T. 2012, *QFitsView: FITS file viewer*, *astrophysics Source Code Library*
- Ouchi, M., Ono, Y., Egami, E., et al. 2009, *ApJ*, 696, 1164
- Overzier, R. A. 2016, *A&A Rev.*, 24, 14
- Palunas, P., Teplitz, H. I., Francis, P. J., Williger, G. M., & Woodgate, B. E. 2004, *ApJ*, 602, 545
- Piqueras, L., Conseil, S., Shepherd, M., et al. 2017 [1710.03554]
- Prescott, M. K. M., Dey, A., & Jannuzi, B. T. 2009, *ApJ*, 702, 554
- Prescott, M. K. M., Dey, A., & Jannuzi, B. T. 2012, *ApJ*, 748, 125
- Prescott, M. K. M., Dey, A., & Jannuzi, B. T. 2013, *ApJ*, 762, 38
- Prescott, M. K. M., Kashikawa, N., Dey, A., & Matsuda, Y. 2008, *ApJ*, 678, L77
- Prescott, M. K. M., Martin, C. L., & Dey, A. 2015a, *ApJ*, 799, 62
- Prescott, M. K. M., Momcheva, I., Brammer, G. B., Fynbo, J. P. U., & Møller, P. 2015b, *ApJ*, 802, 32
- Rakic, O., Schaye, J., Steidel, C. C., & Rudie, G. C. 2011, *MNRAS*, 414, 3265
- Rauch, M., Becker, G. D., & Haehnelt, M. G. 2016, *MNRAS*, 455, 3991
- Remolina-Gutiérrez, M. C. & Forero-Romero, J. E. 2019, *MNRAS*, 482, 4553
- Rivera-Thorsen, T. E., Dahle, H., Chisholm, J., et al. 2019, *arXiv e-prints* [arXiv:1904.08186]
- Rivera-Thorsen, T. E., Dahle, H., Gronke, M., et al. 2017, *A&A*, 608, L4
- Roche, N., Humphrey, A., & Binette, L. 2014, *MNRAS*, 443, 3795
- Rosdahl, J. & Blaizot, J. 2012, *MNRAS*, 423, 344
- Ryabchikova, T., Piskunov, N., Kurucz, R. L., et al. 2015, *Phys. Scr.*, 90, 054005
- Rybicki, G. B. & Loeb, A. 1999, *ApJ*, 520, L79
- Saez, C., Lehmer, B. D., Bauer, F. E., et al. 2015, *MNRAS*, 450, 2615
- Scarlata, C., Colbert, J., Teplitz, H. I., et al. 2009a, *ApJ*, 706, 1241
- Scarlata, C., Colbert, J., Teplitz, H. I., et al. 2009b, *ApJ*, 704, L98
- Schaerer, D. 2013, in *Astrophysics and Space Science Library*, Vol. 396, *Astrophysics and Space Science Library*, ed. T. Wiklund, B. Mobasher, & V. Bromm, 345
- Schirmer, M., Malhotra, S., Levenson, N. A., et al. 2016, *MNRAS*, 463, 1554
- Shibuya, T., Ouchi, M., Konno, A., et al. 2018, *PASJ*, 70, S14
- Shimasaku, K., Kashikawa, N., Doi, M., et al. 2006, *PASJ*, 58, 313
- Skrutskie, M. F., Cutri, R. M., Stiening, R., et al. 2006, *AJ*, 131, 1163
- Smith, A., Ma, X., Broom, V., et al. 2019, *MNRAS*, 484, 39
- Smith, D. J. B., Jarvis, M. J., Simpson, C., & Martínez-Sansigre, A. 2009, *MNRAS*, 393, 309
- Sobral, D., Matthee, J., Darvish, B., et al. 2015, *ApJ*, 808, 139

- Song, M., Finkelstein, S. L., Gebhardt, K., et al. 2014, *ApJ*, 791, 3
- Steidel, C. C., Adelberger, K. L., Dickinson, M., et al. 1998, *ApJ*, 492, 428
- Steidel, C. C., Adelberger, K. L., Shapley, A. E., et al. 2000, *ApJ*, 532, 170
- Steidel, C. C., Adelberger, K. L., Shapley, A. E., et al. 2003, *ApJ*, 592, 728
- Stewart, K. R. 2017, in *Astrophysics and Space Science Library*, Vol. 430, Gas Accretion onto Galaxies, ed. A. Fox & R. Davé, 249
- Stewart, K. R., Maller, A. H., Oñorbe, J., et al. 2017, *ApJ*, 843, 47
- Stobie, R. S. 1980, in *Proc. SPIE*, Vol. 264, Conference on Applications of Digital Image Processing to Astronomy, ed. D. A. Elliott, 208–212
- Stobie, R. S. 1986, *Pattern Recognition Letters*, 4, 317
- Tamura, Y., Kohno, K., Nakanishi, K., et al. 2009, *Nature*, 459, 61
- Taniguchi, Y. & Shioya, Y. 2000, *ApJ*, 532, L13
- Thompson, A. R., Moran, J. M., & Swenson, Jr., G. W. 2017, *Interferometry and Synthesis in Radio Astronomy*, 3rd Edition
- Trainor, R. F., Steidel, C. C., Strom, A. L., & Rudie, G. C. 2015, *ApJ*, 809, 89
- Trebitch, M., Verhamme, A., Blaizot, J., & Rosdahl, J. 2016, *A&A*, 593, A122
- U, V., Hemmati, S., Darvish, B., et al. 2015, *ApJ*, 815, 57
- Umehata, H., Fumagalli, M., Smail, I., et al. 2019, *Science*, 366, 97
- Umehata, H., Matsuda, Y., Tamura, Y., et al. 2017, *ApJ*, 834, L16
- Urrutia, T., Wisotzki, L., Kerutt, J., et al. 2019, *A&A*, 624, A141
- van Hoof, P. A. M. 2018, *Galaxies*, 6, 63
- Vernet, J., Lehnert, M. D., De Breuck, C., et al. 2017, *A&A*, 602, L6
- Villar-Martín, M., Sánchez, S. F., Humphrey, A., et al. 2007, *MNRAS*, 378, 416
- Vio, R. & Andreani, P. 2016, *A&A*, 589, A20
- Wang, P. & Kang, X. 2018, *MNRAS*, 473, 1562
- Weijmans, A.-M., Bower, R. G., Geach, J. E., et al. 2010, *MNRAS*, 402, 2245
- Weilbacher, P. M., Streicher, O., Urrutia, T., et al. 2012, in *Society of Photo-Optical Instrumentation Engineers (SPIE) Conference Series*, Vol. 8451, Society of Photo-Optical Instrumentation Engineers (SPIE) Conference Series, 84510B
- Weilbacher, P. M., Streicher, O., Urrutia, T., et al. 2014, in *Astronomical Society of the Pacific Conference Series*, Vol. 485, Astronomical Data Analysis Software and Systems XXIII, ed. N. Manset & P. Forshay, 451
- Westfall, P. H. 2014, *The American Statistician*, 68, 191
- Yamada, T., Matsuda, Y., Kousai, K., et al. 2012, *ApJ*, 751, 29
- Yang, Y., Decarli, R., Dannerbauer, H., et al. 2012, *ApJ*, 744, 178
- Yang, Y., Zabludoff, A., Eisenstein, D., & Davé, R. 2010, *ApJ*, 719, 1654
- Yang, Y., Zabludoff, A., Jahnke, K., et al. 2011, *ApJ*, 735, 87
- Yang, Y., Zabludoff, A., Tremonti, C., Eisenstein, D., & Davé, R. 2009, *ApJ*, 693, 1579
- Yang, Y., Zabludoff, A. I., Davé, R., et al. 2006, *ApJ*, 640, 539
- Zackay, B. & Ofek, E. O. 2017, *ApJ*, 836, 187
- Zhang, H., Ouchi, M., Itoh, R., et al. 2019, *arXiv e-prints [arXiv:1905.09841]*
- Zheng, Z., Cen, R., Weinberg, D., Trac, H., & Miralda-Escudé, J. 2011, *ApJ*, 739, 62